An Analysis of the Impact of Vertical Wind Shear on Convection Initiation Using Large-Eddy Simulations: Importance of Wake Entrainment

LUKE J. LEBEL[a] AND PAUL M. MARKOWSKI[a]

[a] *Department of Meteorology and Atmospheric Science, The Pennsylvania State University, University Park, Pennsylvania*

(Manuscript received 24 July 2022, in final form 29 March 2023, accepted 31 March 2023)

ABSTRACT: The initiation of thunderstorms in environments characterized by strong wind shear presents a forecast challenge because of the complexities of the interactions between growing cumulus clouds and wind shear. Thunderstorms that develop in such environments are often capable of producing high-impact hazards, highlighting the importance of convection initiation in sheared environments. Although recent research has greatly improved understanding of the structure and evolution of rising thermals in unsheared environments, there remains uncertainty in how wind shear influences the convection initiation process. Two large-eddy simulations (75-m horizontal grid spacing) were performed to study this problem. Convection initiation attempts are forced in the simulations through prescribed surface heat fluxes (the initial boundary layers are statistically horizontally homogeneous and quasi–steady state but contain turbulent eddies as a result of random initial temperature perturbations). The only difference between the two simulations is the presence or absence of wind shear above 2 km. Important differences in the entrainment patterns are present between sheared and unsheared growing cumulus clouds. As found in previous research, the overturning circulation associated with rising thermals drives dynamic entrainment in the unsheared clouds. However, in sheared clouds, wake entrainment resulting from the tilting of environmental vorticity is an important dynamic entrainment pathway. This result has implications for both the structure of sheared growing cumulus clouds and for convection initiation in sheared environments.

SIGNIFICANCE STATEMENT: Forecasts of thunderstorm hazards such as tornadoes, hail, and strong winds, require the accurate prediction of when and where thunderstorms form. Unfortunately, predicting thunderstorm formation is not easy, as there are a lot of different factors to consider. One such factor is environmental vertical wind shear, which describes how winds change speed and direction with height. The purpose of this study is to better understand how wind shear impacts developing clouds. Our results demonstrate a specific mechanism, called "wake entrainment," through which wind shear can weaken developing clouds and potentially prevent them from becoming strong thunderstorms entirely. Understanding this mechanism may be useful for thunderstorm prediction in environments characterized by wind shear.

KEYWORDS: Convective clouds; Deep convection; Wind shear; Cumulus clouds; Entrainment

1. Introduction

The development of thunderstorms, called convection initiation (CI), is a forecast challenge because of its sensitivity to atmospheric features on a multitude of scales. Although CI is often strongly tied to lifting along airmass boundaries (Wilson and Schreiber 1986; Ziegler et al. 1997; Ziegler and Rasmussen 1998; Fovell 2005; Wakimoto and Murphey 2010; Wang et al. 2019), the meso-γ-scale (Orlanski 1975) details frequently are complicated by misocyclones that commonly develop along boundaries (Lee and Wilhelmson 1997a,b; Arnott et al. 2006; Marquis et al. 2007; Buban et al. 2012; Buban and Ziegler 2016; Marquis et al. 2021), as well as interactions between boundaries and horizontal convective rolls (Wakimoto and Atkins 1994; Atkins et al. 1995; Weckwerth et al. 1996; Weckwerth 2000; Xue and Martin 2006a,b) and other modes of boundary layer convection (Peckham et al. 2004). Moreover, vegetation and soil properties (Clark and Arritt 1995), surface flux magnitudes (Segal et al. 1995), surface flux heterogeneity (Kang and Bryan 2011), and terrain (Du et al. 2020) also can influence CI at these small scales.

These meso-γ-scale phenomena and interactions are poorly resolved, if at all, by operational numerical weather prediction models. Therefore, the relationship between CI occurrence and meso-β-scale (Orlanski 1975) environmental characteristics and "ingredients" (Doswell et al. 1996) is often more relevant to the prediction of deep convection at lead times on the scale of hours. CI has been found to be sensitive to large-scale soil moisture anomalies (Barton et al. 2021), low-level moisture (Martin and Xue 2006), midlevel lapse rates (Houston and Niyogi 2007), midlevel relative humidity (Morrison et al. 2020; Peters et al. 2020; Morrison et al. 2022), convective available potential energy (CAPE; Trier et al. 2021), and environmental vertical wind shear (e.g., Peters et al. 2019). Unfortunately, CI can occur in a wide range of atmospheric conditions (Lock and Houston 2014), and therefore a deeper understanding of the mechanisms through which environmental characteristics impact the potential for CI is required.

Given the high-impact hazards that can be produced by thunderstorms in environments characterized by vertical wind shear, it is especially important to understand how wind shear impacts the potential for CI. Previous studies have found that

Corresponding author: Luke J. LeBel, ljl5305@psu.edu

DOI: 10.1175/MWR-D-22-0176.1

wind shear can suppress the initial development of thunderstorm updrafts. Weisman and Klemp (1982) demonstrated this suppression effect in a series of idealized simulations and concluded that the suppression was a consequence of increased entrainment and updraft tilt in strong shear. Supporting this explanation, Lasher-Trapp et al. (2021) documented enhanced entrainment during the developing phase of a simulated supercell thunderstorm, and Parker (2010) demonstrated that tilted updrafts are weaker than upright updrafts as a result of suppressive buoyant perturbation pressure gradient accelerations. In contrast, Peters et al. (2019) found that wind shear suppresses the deepening rate of moist thermals through suppressive dynamic perturbation pressure accelerations, not entrainment-driven buoyancy dilution. These dynamic perturbation pressure accelerations were explained as a consequence of forces analogous to aerodynamic lift. This "shear suppression" effect was subsequently leveraged in the "progressive rooting mechanism" for CI in wind shear (Peters et al. 2022a,b), described below. Therefore, three main ideas exist explaining the suppressive role of wind shear in CI—enhanced buoyancy dilution, buoyant pressure perturbation accelerations, and dynamic perturbation pressure accelerations—and it remains unclear which mechanism is dominant. Adding complexity, Peters et al. (2022a,b) further proposed that wind shear can actually support (and not suppress) CI under certain conditions, demonstrating the need for further research to reconcile these effects.

The progressive rooting mechanism states that "nascent convective updrafts of sufficient width increase their updraft-relative inflow upon encountering environmental wind shear. Updrafts widen because of this increased inflow, which reduces their susceptibility to entrainment-driven dilution. From this process, clouds can progressively 'root' into a deeper steering current, furthering this positive feedback cycle. Updrafts eventually achieve a steady width, w, depth, and motion. Under situations for which progressive rooting occurs, the deleterious effects of shear induced downward pressure gradient accelerations are counteracted" (Peters et al. 2022a,b). The Peters et al. (2022a,b) theoretical model uses many of the results about cumulus cloud structure from recent studies on unsheared convection (e.g., Morrison 2017; Morrison et al. 2020; Peters et al. 2020; Morrison et al. 2022). These studies have greatly advanced understanding of the evolution and structure of unsheared cumulus convection, and in particular have demonstrated the importance of dynamic entrainment associated with the toroidal circulations of rising thermals in determining the properties and structure of unsheared deepening clouds. However, observations and simulations demonstrate that there are fundamental differences in flow structures between sheared and unsheared convection (e.g., Cotton and Tripoli 1978), and therefore the application of results from studies on unsheared convection to sheared convection may not be straightforward. Notably, different dynamic entrainment mechanisms are active in the presence of shear. Lasher-Trapp et al. (2021) examined entrainment in a simulated developing supercell thunderstorm and identified the presence of a strengthened overturning circulation (a "P-type thermal circulation"; Kitchen and Caughey 1981) on the downshear side of the deepening cloud. It will be demonstrated herein that an additional entrainment pattern, known as wake entrainment (Knupp and Cotton 1985), plays an important role in sheared deepening cumulus convection.

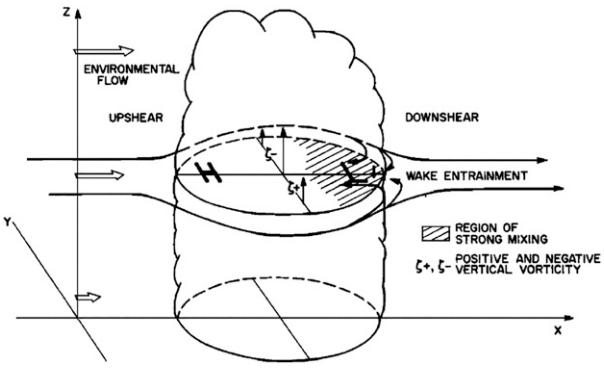

FIG. 1. A schematic diagram from Knupp and Cotton (1985) illustrating wake entrainment in a sheared cloud.

Wake entrainment is an asymmetric type of dynamic entrainment, in which drier and potentially cooler air is incorporated into the downshear side of an updraft (Kingsmill and Wakimoto 1991). Although Houze (2014) defined "dynamic entrainment" as that which satisfies mass continuity, the term more commonly is used to describe entrainment that results from *cloud-scale* flow structures (Morrison et al. 2020). It therefore is distinguished from entrainment driven by small-scale turbulent eddies (e.g., Houze 2014; Morrison et al. 2020). In other words, one can define dynamic entrainment as cloud-scale entrainment that is independent of the development or intensity of turbulence, whereas eddy entrainment is driven by turbulent eddies and therefore is ultimately driven by hydrodynamical instabilities (static instability, shear instability). Dynamic entrainment can result both from overturning thermal circulations (e.g., Morrison et al. 2020; Peters et al. 2022a) and from vertical vortices, as in wake entrainment. Wake entrainment occurs as a result of the tilting of horizontal vortex lines associated with environmental vertical wind shear. The resulting vortex pair that straddles the updraft produces cloud-scale inflow (i.e., entrainment) on the downshear side of cumulus convection (Fig. 1; Knupp and Cotton 1985; Wakimoto 2001). Vortex pairs have been identified in several studies to rapidly develop in sheared cumulus convection (Cotton and Tripoli 1978; Dahl 2017), and observations support the enhanced dilution (Heymsfield et al. 1978) and associated downdraft formation (Knupp and Cotton 1982) on the downshear side of sheared clouds. In idealized simulations, Tripoli and Cotton (1980) found that robust dynamic entrainment through a process similar to wake entrainment resulted in the erosion of the low-level updraft and the eventual dissipation of a simulated convective cell, suggesting that wake entrainment may play an important role in the initiation of sustained deep convection. The role of wake entrainment in CI has not been thoroughly examined in more recent research.

The purpose of this article is to further explore the effects of vertical wind shear above the boundary layer on CI, using

large-eddy simulations. Despite recent advances, there remains uncertainty in the mechanism through which wind shear influences the potential for CI, and in how the results from previous studies can be applied to real world sheared CI scenarios. It is hypothesized that wake entrainment enhances dilution in sheared deepening clouds, and moreover that wake entrainment can result in CI failure in sheared environments. The specifics of the large-eddy simulation framework are discussed in section 2. Sections 3 and 4 contain the results of the large-eddy simulations and associated sensitivity tests, respectively. A discussion of the results in the context of previous work is presented in section 5, and final conclusions are shared in section 6.

2. Methods

Large-eddy simulations were performed using Cloud Model, version 1 (CM1; Bryan and Fritsch 2002), release 18.3. CM1 is an open-source atmospheric model that is widely used in the analysis of thunderstorms and CI (e.g., Peters et al. 2019, 2020; Lasher-Trapp et al. 2021). The specific model configuration used in this study is identical to that in Markowski (2020) except for the forcing mechanism for CI. The reader is therefore referred to Markowski (2020) for a complete documentation of the model configuration, and only a few noteworthy aspects are discussed here.

The model horizontal grid spacing is 75 m, which is comparable to that used in recent simulations examining the role of wind shear on CI [e.g., 100 m used by Peters et al. (2019) and Lasher-Trapp et al. (2021)]. A notable exception is the simulation of a growing cumulus congestus cloud presented by Strauss et al. (2022), which used a horizontal grid spacing of 5 m. There are 121 vertical levels, and the vertical grid spacing varies from 15 m at the surface to 285 m near the domain top of 18 015 m. The model domain spans 127.5 km in both the x and y directions (1700 × 1700 grid points). The lateral boundary conditions are periodic. The lower boundary condition is semi-slip, with a roughness length of 0.12 m. The National Severe Storms Laboratory (NSSL) double-moment microphysics (Mansell et al. 2010) is used, and subgrid-scale turbulence is parameterized using a turbulent kinetic energy (TKE) scheme similar to Deardorff (1980). Simulations were initially performed for a 12-h spinup period, to allow for the development of nearly steady-state, sheared, turbulent boundary layer. Random potential temperature perturbations with a maximum amplitude of 0.25 K were inserted below 1 km at $t = 0$ h to initiate the development of turbulence, and no surface heat fluxes were prescribed during the spinup period. Markowski (2020) discusses the implications of this spinup period; the domain mean temperature, dewpoint, and winds at the conclusion of the spinup period are presented in Fig. 2.

Two simulations are analyzed to determine the impact of wind shear on CI. Both simulations use the thermodynamic base state from Markowski (2020), which is a modified version of the Weisman and Klemp (1982) profile and is characterized by large CAPE and minimal convective inhibition (CIN; Fig. 2). The first simulation (hereinafter, the "SHEAR" simulation) additionally uses the wind profile from Markowski (2020),

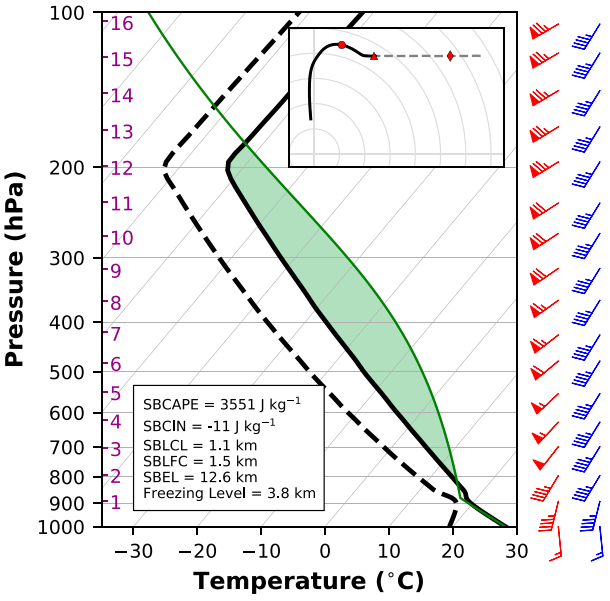

FIG. 2. A skew T–log$p$ diagram depicting the domain mean temperature (black, solid), dewpoint (black, dashed), and surface-based parcel profile temperature (green) at $t = 12$ h after the spinup period. The light-green shaded area is the region of CAPE for a surface-based parcel. The wind barbs indicate wind speed (kt; 1 kt ≈ 0.51 m s^{-1}) and direction in the SHEAR (red) and NOSHEAR2 (blue) simulations at the closest model level to each whole kilometer up to $z = 16$ km. Heights above the surface (km) are indicated with magenta text. The inset diagram displays the associated hodograph, with the black line indicating the 0–2-km winds present in the base state of both simulations, and the gray dashed line indicating the winds above 2 km present only in the SHEAR base state. The red circle, triangle, and diamond indicate the winds in the SHEAR simulation at $z = 1$, 2, and 8 km, respectively. Rings are shown every 10 kt. The inset text indicates the surface-based (SB) CAPE, CIN, LCL, LFC, and equilibrium level (EL), along with the freezing level of the profile.

which is characterized by strong vertical wind shear over the lowest 8 km. The shear from the surface to 2 km is predominantly southerly, and from 2 to 8 km, westerly (the magnitude of the 0–2-km bulk shear is 18.2 m s^{-1}, and the magnitude of the 2–8 km bulk shear is 15.5 m s^{-1}; Fig. 2). As demonstrated by Markowski (2020), the SHEAR environment supports tornadic supercell thunderstorms assuming sustained CI. The second simulation (hereinafter, the "NOSHEAR2" simulation) uses the same wind profile below 2 km, but constant winds above 2 km. The NOSHEAR2 environment supports multicellular thunderstorms with transient supercellular structures, based on a 1.5-h simulation in which a large warm bubble was used to initiate storms. A comparison of the SHEAR and NOSHEAR2 simulations, therefore, allows for an examination of the role of wind shear above 2 km in the CI process.

CI "attempts" [defined as parcels surpassing their level of free convection (LFC)] are forced in the simulations using a prescribed corridor of surface sensible heat fluxes. This definition of CI attempts is less strict than common definitions for CI. For example, Peters et al. (2022a) define "deep convection

initiation" as "the onset of cumulonimbus convection." The language of CI attempts is used here as the clouds that deepen past their LFC have the opportunity to produce cumulonimbus convection. Moreover, from an societal impacts perspective, it may be appropriate for definitions of CI to involve criteria of storm intensity and longevity (e.g., Kain et al. 2013). We therefore further use the language of CI "success" and "failure" in the context of CI attempts. CI success refers to the development of long-lived, sustained, precipitating convection from a given CI attempt, and CI failure occurs when such long-lived, precipitating convection does not form. A similar language choice is made by Nelson et al. (2021), where a distinction between "initiation of sustained convection" and "failed convection initiation" is made based on the magnitude and persistence of radar reflectivity echoes.

Following a method similar to that of Rousseau-Rizzi et al. (2017) and Tang and Kirshbaum (2020), a surface sensible heat flux $H(x, t)$ is prescribed beginning after the 12-h period of model spinup via

$$H(x, t) = H_0 \exp\left\{-\frac{[x - x_0 - u_d(t - 43\,200)]^2}{a^2}\right\}, \quad (1)$$

where $H_0 = 0.2$ K m s^{-1} is the maximum sensible heat flux, $x_0 =$ 30 km determines the initial forcing position, $a = 7.5$ km controls the width of the heating region, t is the simulation time in seconds, and $u_d = -12.2$ m s^{-1} is required to offset the eastward component of the northeastward domain translation (Markowski 2020) and allow the forcing to remain stationary in a ground-relative reference frame. Over time, the prescribed surface sensible heat fluxes result in the development of a boundary layer circulation that supports CI attempts.

Dozens of CI attempts occur within the domain during the 2-h simulations. To examine the population of clouds produced in the simulations, cloud objects are then identified in the simulations as coherent regions of total cloud water mixing ratio > 0.01 g kg^{-1} and vertical velocities > 3 m s^{-1}. To examine the dilution of these cloud objects during CI attempts, two layers of passive tracers with maximum values of 1 g kg^{-1} are inserted into the simulated environment after the model spinup period at $t = 12$ h. As in Lasher-Trapp et al. (2021), one passive tracer (hereinafter, PT1) is distributed uniformly from the surface to the lifting condensation level (LCL; 1.1 km) to examine the dilution of air ingested below cloud base. The second passive tracer (PT2) is distributed uniformly between the LCL and 2 km. The combination of both tracers (PT1 + PT2) results in an initially uniform tracer concentration of 1 g kg^{-1} below 2 km. PT1 + PT2 concentrations are therefore used to examine the variations in dilution that occur in simulated cloud objects as a result of differences in shear above 2 km.

3. Results: Idealized simulations

Several CI attempts occur in both the SHEAR and NOSHEAR2 simulations. By $t = 13$ h, isolated deepening clouds with cloud-top heights > 5 km are present in both simulations (Figs. 3a,c). These early CI attempts are slightly more common in the NOSHEAR2 simulation, suggesting that the timeline of CI is slightly delayed in the presence of shear. By $t = 14$ h, deep clouds are widespread in both simulations (Figs. 3b,d). Numerous CI attempts therefore occur in the period from $t = 13$ to 14 h, and this period will be the focus of the following analysis. Data were output from the simulations each minute during this period. In section 3a, we examine the mean vertical profiles of cloud object properties. In section 3b, spatial composites are calculated to explain the differences in cloud object properties between the SHEAR and NOSHEAR2 simulations. In section 3c, individual sample cloud objects are identified from each simulation to assess the applicability of the composite results to CI attempts.

a. Composites: Bulk properties

To analyze the effects of wind shear on the CI process, the bulk properties of each population of ascending clouds are first calculated and compared. A subset of cloud objects that have a base below 2 km and a top between 4 and 4.5 km was selected to examine the differences between the simulated cloud populations. These objects were selected to represent a subset of newly deepening clouds; the results presented here are not sensitive to small changes in the selected range of cloud object top heights. To examine the differences between the simulated cloud object populations, the mean values of cloud object properties at each model level were calculated within individual cloud objects, aggregated within each simulation, and then compared.

There are notable differences in the resulting distributions of cloud properties between the SHEAR and NOSHEAR2 simulations. The cloud objects reaching the 4–4.5-km level are slightly larger in upper portions of the cloud in the SHEAR simulation than in the NOSHEAR2 simulation (Fig. 4a). In addition, the mean updraft speeds are significantly larger near the cloud top in the NOSHEAR2 simulation (Fig. 4b). Peters et al. (2019) found that thermals rise more slowly in the presence of shear, in agreement with this result. Consistent with the stronger mean updraft, the mean potential temperature perturbation θ' is also larger in the NOSHEAR2 cloud objects (Fig. 4c). The mean tracer distributions suggest an important relationship between dilution and the maintenance of a buoyant updraft. Both cloud object populations exhibit large decreases, and therefore dilution, of PT1 and PT1 + PT2 with height (Figs. 4d,e), consistent with the deviation of the potential temperature perturbations from a surface-based parcel with height (Fig. 4c). However, dilution is significantly larger in the SHEAR cloud population than the NOSHEAR2 cloud population for both PT1 and PT1 + PT2 concentrations (Figs. 4d,e), especially near cloud top. These results support the hypothesis that entrainment is more effective at diluting cloudy updrafts in the presence of shear, and these differences in dilution may have impacts on the potential for sustained CI.

b. Spatial composites

The composite bulk properties demonstrate that deepening clouds in sheared environments experience enhanced dilution. However, the mean profiles do not explain the entrainment

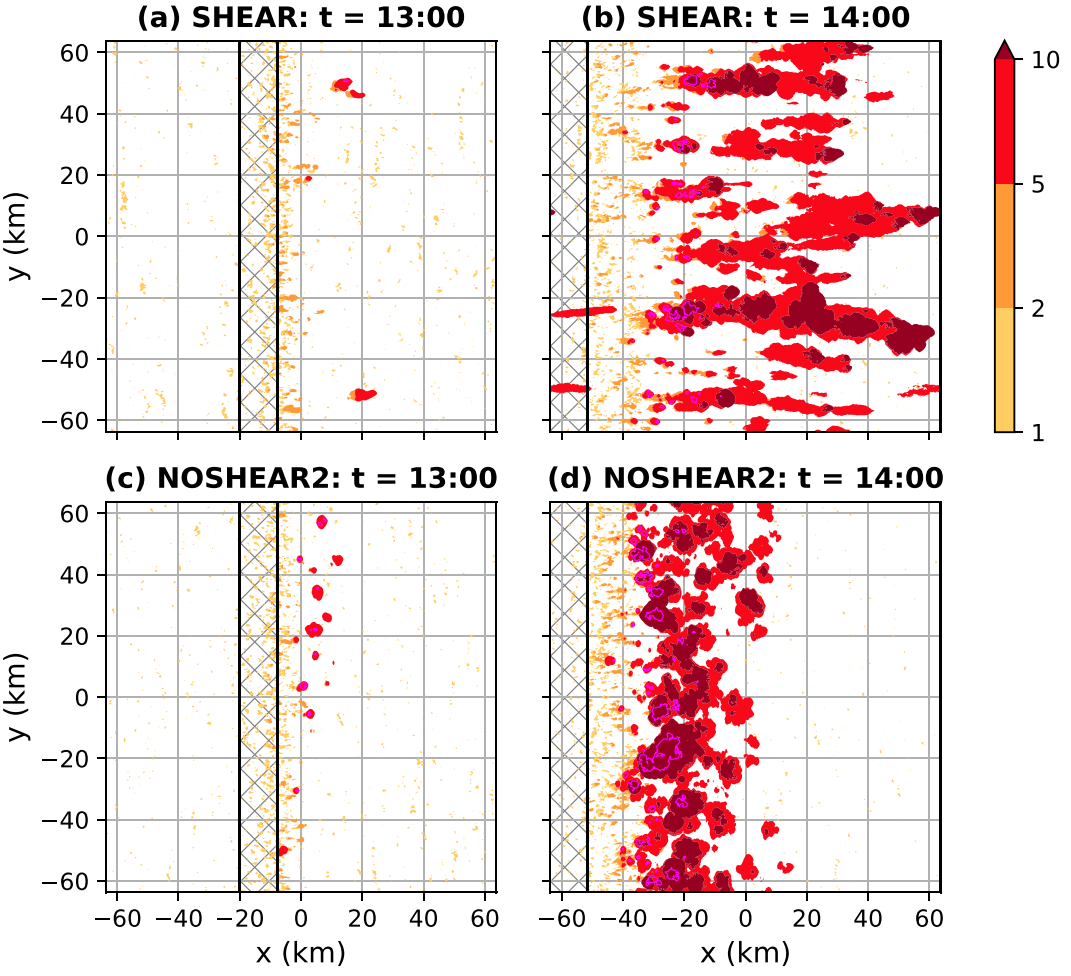

FIG. 3. Cloud-top height (km) in the (a),(b) SHEAR and (c),(d) NOSHEAR2 simulations at (left) $t = 13$ and (right) $t = 14$ h. The black hatched region indicates the location of surface sensible heat flux greater than 0.1 K m s^{-1}. The magenta contours outline the regions with ≥1 g kg^{-1} column maximum precipitation mixing ratio. Note that the domain itself translates to the northeast; the forcing is in a fixed location relative to the ground.

mechanism resulting in enhanced dilution in sheared clouds. To investigate the mechanisms, a spatial composite mean was calculated for both the SHEAR and NOSHEAR2 simulations using the same subset of cloud objects (cloud base below 2 km, cloud top between 4 and 4.5 km). The composites are calculated relative to the maximum updraft helicity within the cloud footprint (smoothed using a Gaussian filter with standard deviation = 1 point) at the vertical level of the composite. This method was used (as opposed to compositing relative to the more nebulous cloud centroid, for example) to provide a physically meaningful "anchor" for the spatial composite calculations. The sample sizes are slightly smaller than in the previous section, as a small number of the cloud objects that were close to the edge of the model domain were excluded from the spatial composites for convenience.

At $z = 3$ km (near the midpoint between cloud base and cloud top), large differences in flow structures are apparent between the composite means. In the SHEAR simulation, strong counterrotating vortices (Fig. 5c) are present on the flanks of the composite mean updraft (maximum $w = 7$ m s^{-1}). These vortices originate from the tilting of horizontal vorticity associated with the environmental vertical wind shear into the vertical and its subsequent upward advection and stretching, and result in an asymmetric "C"-shaped pattern in PT1 + PT2 concentration throughout the composite updraft (Fig. 5a). In the NOSHEAR2 simulation, however, the composite mean updraft (maximum $w = 7$ m s^{-1}) is associated with a large, relatively symmetric region of high PT1 + PT2 tracer concentrations (Fig. 5d). Much weaker counterrotating vortices are apparent in the NOSHEAR2 composite mean than in the SHEAR composite mean (Figs. 5f,i), and develop in response to the presence of environmental wind shear below 2 km. The difference between the two composite means reveals that the SHEAR simulation has significantly larger PT1 + PT2 concentrations on the upshear side and lateral flanks of the updraft, and significantly lower PT1 + PT2 concentrations within the center of the cloud

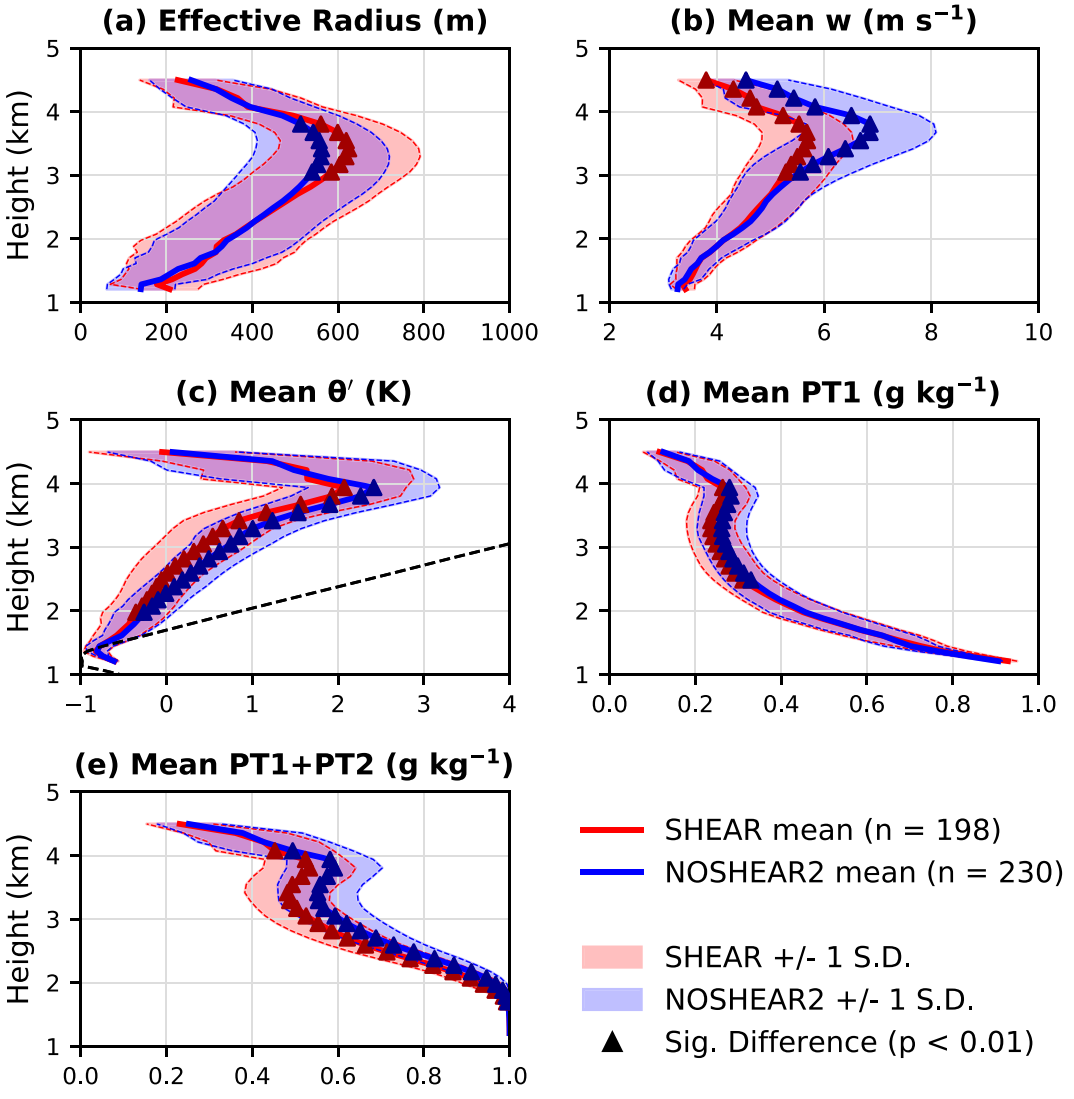

FIG. 4. A comparison of cloud properties within the SHEAR (red) and NOSHEAR2 (blue) simulations. Cloud properties include (a) effective radius [calculated as $\sqrt{(\text{area}/\pi)}$], (b) mean vertical motion, (c) mean θ', and (d) mean PT1 and (e) mean PT1 + PT2 concentrations. The shaded region extends ±1 standard deviation from the mean. The black dashed line in (c) displays the θ' of the surface-based parcel in Fig. 2. Triangles indicate the levels where the distributions are significantly different at the 1% significance level, according to a Welch's *t* test.

(Fig. 5g). Averaging within the composite mean 3 m s^{-1} vertical velocity isotach, the SHEAR simulation has 0.086 g kg^{-1} lower tracer concentration than the NOSHEAR2 simulation (recall that the initial concentration of PT1 + PT2 below 2 km is 1 g kg^{-1}). This represents an 18.3% decrease in updraft ($w >$ 3 m s^{-1}) PT1 + PT2 concentration in the SHEAR simulation relative to the NOSHEAR simulation. This difference in dilution is attributed to the wake entrainment mechanism that results from the strong counterrotating vortices within the SHEAR composites.

The difference in PT1 + PT2 dilution between the SHEAR and NOSHEAR2 composites has implications for updraft buoyancy (B). Throughout this paper, buoyancy is calculated using the formulation from CM1 (Bryan and Fritsch 2002):

$$B = g\left[\frac{\theta - \overline{\theta}}{\overline{\theta}} + \left(\frac{R_v}{R_d} - 1\right)(q_v - \overline{q}_v) - (q_t - q_v)\right], \qquad (2)$$

where $\overline{\theta}$ is the base state potential temperature, $\overline{q}_v$ is the base state water vapor mixing ratio, q_v is the water vapor mixing ratio, q_t is the total water mixing ratio, and R_v and R_d are the gas constants for water vapor and dry air, respectively. In the SHEAR simulation, positive buoyancy is confined to the upshear flanks of the updraft and within the counterrotating vortices (Fig. 5b), and negative buoyancy is present within

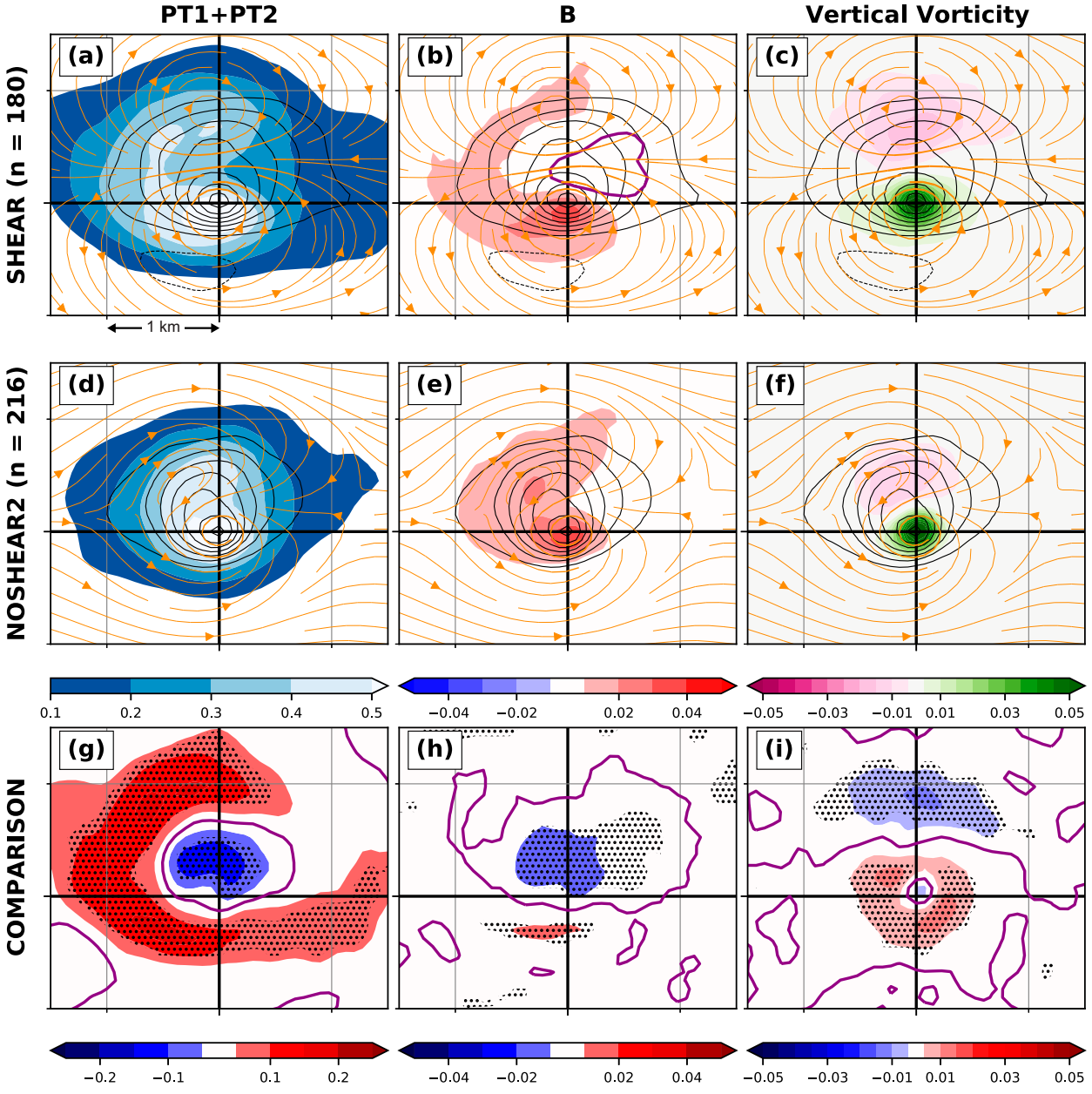

FIG. 5. Composite mean values for the (a)–(c) SHEAR and (d)–(f) NOSHEAR2 simulations at the model level closest to $z = 3$ km (model level 47). The shading in (a) and (d) indicates PT1 + PT2 concentration (g kg^{-1}), the shading in (b) and (e) indicates buoyancy (m s^{-2}), and the shading in (c) and (f) indicates vertical vorticity (s^{-1}). Vertical velocity (black contours, every 1 m s^{-1}) and perturbation winds (orange streamlines, relative to the $t = 12$ h base state) appear in all panels. Dashed black contours indicate negative vertical velocities. Also shown is the difference (SHEAR − NOSHEAR2) between (g) the mean PT1 + PT2 concentration, (h) buoyancy, and (i) vertical vorticity, with stippling indicating statistical significance ($p < 0.001$) according to a Welch's t test. The purple line in (b), (g), (h), and (i) indicates the zero isopleth.

downshear portions of the cloud. The source of this region of negative buoyancy is discussed later in section 4b. In the NOSHEAR2 simulation, there is a large region of positive buoyancy within the upshear portion of the updraft and between the vortices (Fig. 5e; as discussed above, the shear below 2 km can explain the weak counterrotating vortices in the NOSHEAR2 composite). A comparison of the buoyancy values reveals that the SHEAR composite is significantly less buoyant within a large region of the composite mean updraft, demonstrating the efficiency of wake entrainment at diluting the buoyancy within sheared updrafts. Within the composite mean updraft, the SHEAR simulation has a mean buoyancy

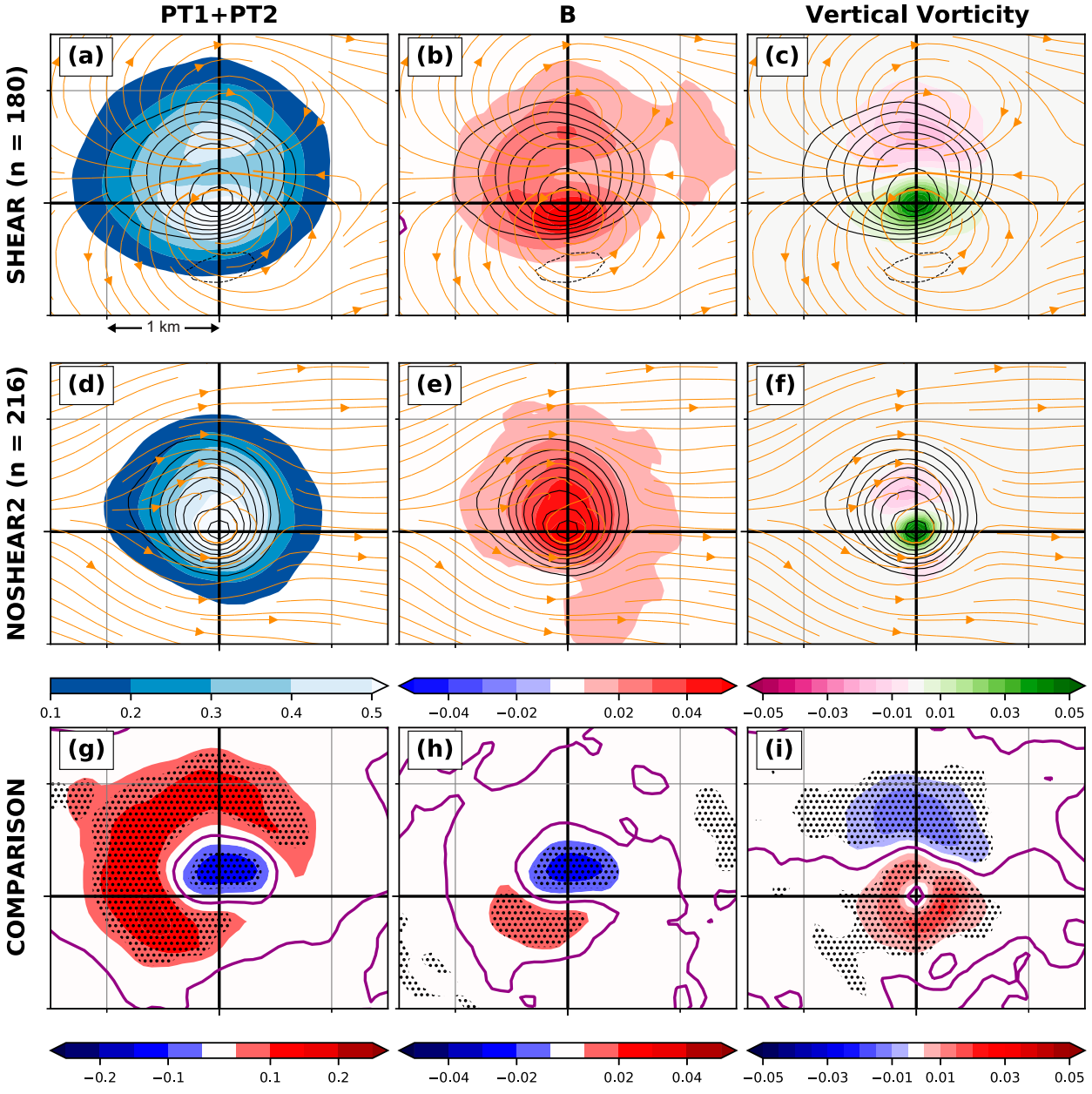

FIG. 6. As in Fig. 5, but for the model level closest to $z = 3.5$ km (model level 51).

value 0.012 m s^{-2} lower than in the NOSHEAR simulation, representing a decrease of 61.5% relative to the NOSHEAR composite mean.

At slightly higher altitudes in the composite mean cloud ($z = 3500$ m), a similar pattern is apparent. In the SHEAR composite, two local maxima in PT1 + PT2 concentration exist on both sides of the composite mean updraft (maximum vertical velocity $w = 7$ m s^{-1}; Fig. 6a). These maxima correspond to the two counterrotating vortices that laterally bound the updraft and confirm the dominance of the wake entrainment mechanism in the composite mean. In the NOSHEAR2 composite, the PT1 + PT2 concentration is high (>0.5 g kg^{-1}) in the center of the updraft (maximum $w = 8$ m s^{-1}; Fig. 6d). A comparison of the PT1 + PT2 composite values indicates that the SHEAR cloud population has significantly larger PT1 + PT2 concentrations upshear and within the counterrotating vortices, while the NOSHEAR2 cloud population has significantly larger PT1 + PT2 concentrations within the center of the cloud. Notably, the PT1 + PT2 concentration is 0.041 g kg^{-1} lower within the 3 m s^{-1} updraft isotach in the SHEAR simulation than in the NOSHEAR2 simulation, representing an 8.9% decrease in updraft PT1 + PT2 concentration in the SHEAR composite mean relative to the NOSHEAR2 composite mean.

Once again, these differences in dilution impact the buoyancy of the composite mean clouds. Unlike in the $z = 3000$ m composites, both the SHEAR and NOSHEAR2 composite updrafts at $z = 3500$ m have positive buoyancy throughout. However, the spatial distribution of buoyancy is different between the cloud populations. In the SHEAR cloud, the highest buoyancy values are upshear and on the flanks of the cloud within the counterrotating vortices (Fig. 6b), consistent with the PT1 + PT2 distribution. In the NOSHEAR2 cloud, the highest buoyancy values are collocated with the maximum vertical velocities (Fig. 6e). As a result, the SHEAR composite has significantly higher buoyancy on the southern flank of the updraft and significantly lower buoyancy north of the composite mean updraft maximum within the center of the cloud (Fig. 6h). In fact, the SHEAR composite is 0.008 m s^{-2} less buoyant within the 3 m s^{-1} updraft isotach. This is a 22.2% decrease in updraft buoyancy in the SHEAR composite relative to the NOSHEAR2 composite, emphasizing the effectiveness of wake entrainment.

c. *Analysis of particular clouds*

The composite means demonstrate that wake entrainment is effective at diluting the updraft of sheared clouds. To examine how this entrainment mechanism is manifest in a specific cloud (and to examine the applicability of the composite means to individual clouds), an example cloud object was selected from each simulation. The example clouds were identified at the same simulation time of $t = 13$ h 10 min and have similar cloud-top heights between 4 and 4.5 km, and therefore are in a similar stage of CI. Comparing the three-dimensional characteristics of the example clouds (Fig. 7) reveals large differences between the clouds. In the example cloud from the SHEAR simulation, there is a single dominant tilted updraft within the cloud (Fig. 7a). An arching vortex line (approximated by the orientation of the vorticity isosurface in Fig. 7a) associated with counterrotating vertical vortices straddles the tilted updraft, suggesting an important role of the tilting and stretching of environmental vorticity. The vorticity vectors on opposite sides of the updraft are in opposite directions (not shown), and the resulting implied inflow on the downshear side of the updraft is consistent with the wake entrainment mechanism identified in the SHEAR composite mean. In the example cloud from the NOSHEAR2 simulation, there is again a dominant rising updraft (Fig. 7b). The vorticity field associated with this updraft is characterized by a vortex ring around the updraft, suggesting that the overturning toroidal circulation associated with the ascending thermal-like updraft is the dominant storm-scale flow structure.

Encouragingly, the sample clouds display a similar pattern (Fig. 8) to the spatial composite means. At $z = 3.5$ km, the sample SHEAR cloud is clearly suffering from wake entrainment. There are two maxima of PT1 + PT2 concentrations, collocated with strong counterrotating vortices (Fig. 8a). These PT1 + PT2 concentration maxima correspond with maxima in buoyancy as well (Fig. 8b). Moreover, within the region of wake entrainment between the counterrotating vortices there is actually a region of negative buoyancy, evidence

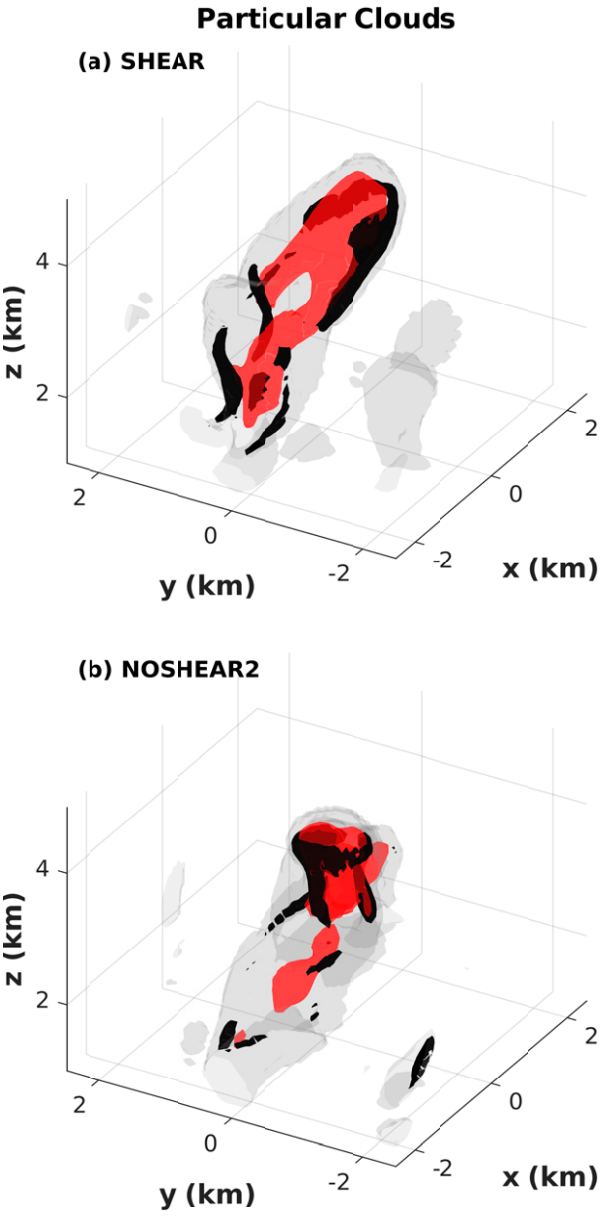

FIG. 7. Three-dimensional isosurfaces of total cloud water mixing ratio (0.01 g kg^{-1}; light gray), upward vertical velocity (5 m s^{-1}; red), and three-dimensional vorticity magnitude (0.06 s^{-1}; black) for an example storm in (a) the SHEAR simulation and (b) the NOSHEAR2 simulation. The x and y coordinates are in kilometers from the storm centroid. Recall that the shear vector above 2 km is in the positive x direction for the SHEAR simulation. The clouds are viewed from the southwest at an elevation angle of 30°.

of the effectiveness of the wake entrainment mechanism. On the other hand, the sample NOSHEAR2 cloud is associated with a spatially compact updraft characterized by high PT1 + PT2 concentration and high buoyancy (Figs. 8d,e). There is relatively weak and disorganized horizontal flow within the sample NOSHEAR2 cloud, suggesting that the $z = 3.5$ km level is near or slightly below the midpoint of the thermal

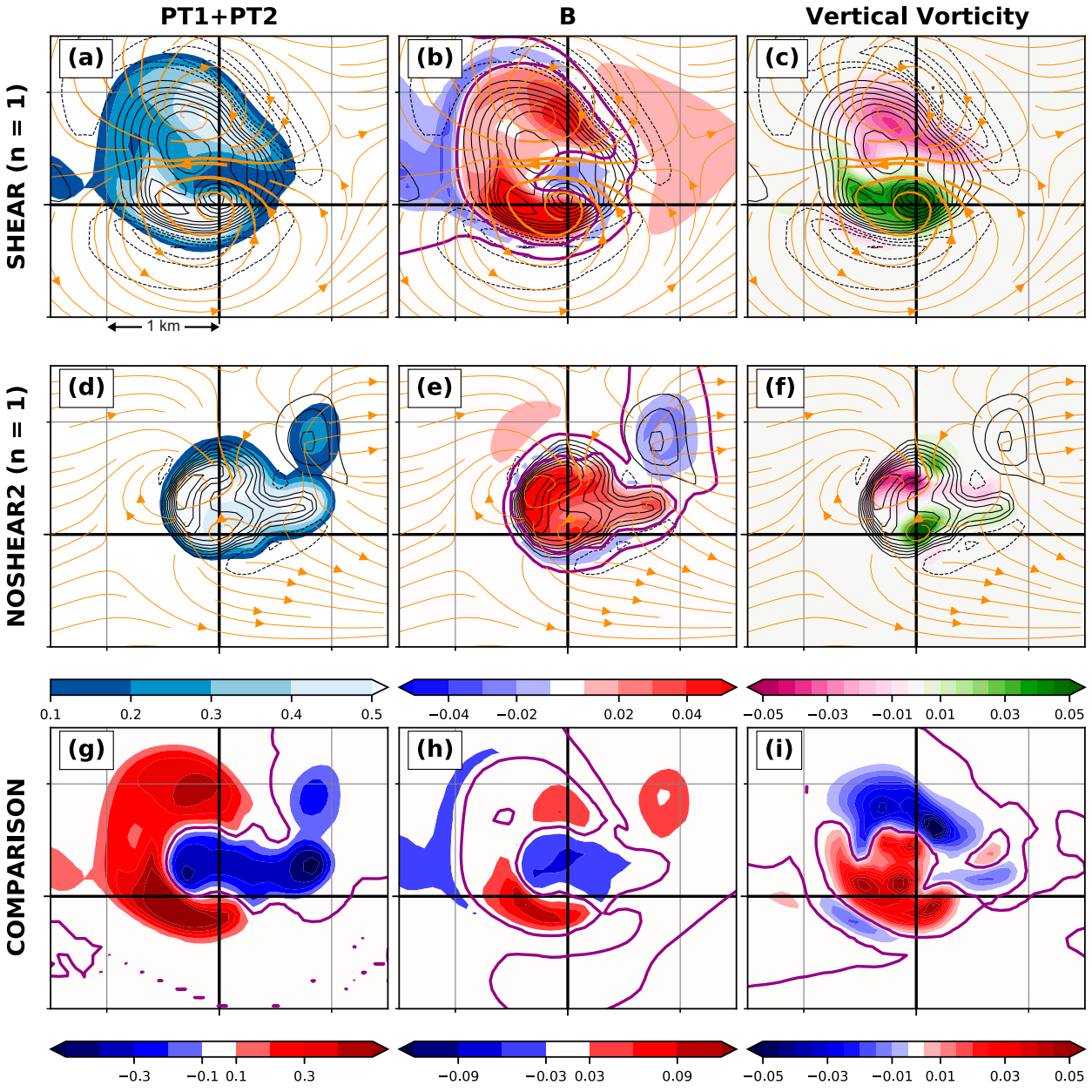

FIG. 8. As in Fig. 5, but for the particular clouds referenced in section 3c at the model level closest to 3.5 km. Note that the color bars used in (g) and (h) differ from those in Figs. 5 and 6.

element apparent in Fig. 7b. A comparison between the SHEAR and NOSHEAR2 simulation (Figs. 8g,h,i) highlights the lower PT1 + PT2 concentrations and buoyancy values near the center of the cloud in the SHEAR simulation. In fact, the mean PT1 + PT2 concentration within the area enclosed by the 3 m s^{-1} vertical velocity isotach is 0.085 g kg^{-1} lower within the SHEAR simulation than in the NOSHEAR2 simulation (a percent decrease of 17.9% of PT1 + PT2 concentration in the SHEAR updraft relative to the NOSHEAR2 updraft), which is evidence of strong dilution. Moreover, the SHEAR simulation has a mean buoyancy value within the 3 m s^{-1} vertical velocity isotach that is 0.008 m s^{-1} lower than in the NOSHEAR2 simulation (a percent decrease of 23.5% of buoyancy in the SHEAR updraft relative to the NOSHEAR updraft), emphasizing that the entrainment and dilution has a nonnegligible effect on buoyancy. It is worth mentioning that additional regions of negative buoyancy exist upshear ("west") of the SHEAR sample cloud and to the downshear left ("northeast") of the NOSHEAR2 sample cloud that are not present in the composite means. These features are associated with other neighboring updrafts, and the effects of these neighboring updrafts are averaged out in the spatial composites.

4. Results: Warm bubble sensitivity tests

Despite the numerous CI attempts in both the SHEAR and NOSHEAR2 simulations, intense, long-lived, precipitating storms failed to develop. The reasons for this failure warrant further investigation, particularly because such storms developed in the Markowski (2020) simulations. Markowski (2020) used an identical thermodynamic environment and wind profile to the SHEAR simulation, and accomplished CI of long-lived supercell thunderstorms by introducing a large warm bubble into a quasi-steady turbulent boundary layer. Although no long-lived storms developed in the simulations analyzed in section 3, air parcels routinely reached their LFC, achieved significant buoyancy, and reached high altitudes (>10 km; Fig. 3). Therefore, long-lived storms failed to develop in the simulations because all deepening clouds became disconnected from the CAPE-rich boundary layer. In this light, the CI failure herein can be described as a "bottom up" process. One hypothesis explaining this CI failure is that the developing clouds were narrow and therefore highly susceptible to the deleterious effects of wake entrainment. In this hypothesis, wake entrainment dilutes and eventually splits developing updrafts near cloud base. The updrafts resulting from the split are spatially small and therefore susceptible to further entrainment and dilution via both cloud-scale flow structures and turbulent eddies. As a consequence of this continued dilution, the updrafts weaken and become disconnected from the CAPE-rich boundary layer.

a. Sensitivity to warm bubble size

To examine this hypothesis, a series of simulations were conducted using warm bubbles with different horizontal radii R_H inserted into the SHEAR base state. All warm bubbles are centered at $z = 1.4$ km, have a vertical radius of 1.4 km, and have maximum θ perturbations of 2.0 K. The results from simulations with R_H of 1.5, 2.0, 2.5, 3.0, 3.5, and 4.0 km are presented here. It is well established that warm bubbles do not accurately reflect real-world CI (e.g., Loftus et al. 2008; Lasher-Trapp et al. 2021). Warm bubbles used to force CI in thunderstorm simulations are typically much larger than thermals within a convective boundary layer, and therefore do not replicate a real-atmosphere CI mechanism (Loftus et al. 2008). Moreover, Lasher-Trapp et al. (2021) found that simulated clouds produced by warm bubbles can experience less entrainment relative to clouds produced by other methodologies. Because of these known limitations, the goal of this sensitivity test is to use warm bubbles as a tool to gain insight into the CI process, and not to make specific quantitative conclusions about the updraft size thresholds for CI. The use of warm bubbles in this manner is further supported by the structural similarities between the most robust CI attempts forced by surface heat fluxes in the SHEAR simulation and simulated CI attempts forced by the 1.5-km radius warm bubble (Fig. 9). Because simulations using warm bubbles can reproduce the development of a wake entrainment mechanism and the associated dilution and buoyancy characteristics, they can be useful to gain insight into the success and failure of CI.

The warm bubble simulations produce clouds of varying width, allowing for the systematic examination of the role of initial cloud width on sustained CI success. The smallest radius ($R_H = 1.5$ km) warm bubble produces a cloud that is structurally similar to the most robust CI attempts in the SHEAR simulation (Fig. 9). As in the SHEAR simulations, the CI attempt within the $R_H = 1.5$-km simulation fails by 30 min after the bubble was inserted into the model (Fig. 10). This failure occurs as the rising bubble detaches from the boundary layer, consistent with a bottom-up failure mechanism. This evolution is demonstrated in Fig. 11. The warm bubble quickly results in the development of a cloud, and the cloudy updraft initially is characterized by relatively undiluted air that originates below the LCL (Figs. 11a,b). However, by $t = 12$ min after bubble insertion, the cloudy updraft is becoming increasingly diluted (Fig. 11d), and by $t = 18$ min after bubble insertion the cloud is no longer attached to the boundary layer (Fig. 11f; note the separation in cloudy regions between $z = 2$ and 3 km) and the updraft is weakening (Fig. 10). This CI failure occurs despite the cloud top reaching well above 8 km. The simulation with $R_H = 2.0$ km also fails by 30 min into the simulation (Fig. 10; note that a secondary updraft is deepening at $t = 30$ min after the bubble was inserted, but this updraft is weak and diluted). Further increases in R_H result in successful CI. Increasing R_H to 2.5 km results in a pulsing updraft that lasts through the entire 90-min simulation with maximum updraft speeds commonly near 30 m s^{-1}. A R_H value of 3.0 km results in a storm that maintains and intensifies, and even larger values of R_H produce wider and more rigorous updrafts. This result supports the hypothesis that the relatively small updrafts produced in the SHEAR simulation were too narrow for sustained CI.

Even in the warm bubble simulations with successful CI, the role of wake entrainment is apparent. To assess the role of wake entrainment, the $R_H = 2.5$-km simulation will be used. The other bubble sizes, including the $R_H = 1.5$-km simulation (see Fig. 9), have qualitatively similar evolutions. Then, 10 min after the bubble was inserted into the SHEAR base state, the simulated cloud had deepened to over 7 km (Fig. 12a). A horizontal cross section near $z = 5$ km indicates that the cloud is experiencing strong wake entrainment below cloud top (Figs. 12c,d). The region of high PT1 + PT2 concentration is confined within a C-shaped region on the upshear side of the cloud and within two counterrotating updrafts (Fig. 12c). In the interior of the cloud, a large region of negative buoyancy with vertical motion > 10 m s^{-1} is present. In fact, this negatively buoyant updraft is present through much of the cloud, as apparent by the crescent shape of negative buoyancy on the downshear side of the cloud in a x–z plane (Fig. 12b). At 12 min after the bubble was inserted, a similar flow structure remained (Fig. 13), emphasizing the persistence of the wake entrainment mechanism during the early stages of CI. In the x–y plane at $z = 5$ km, two counterrotating vortices are again present, and the high tracer concentrations remain confined to the upshear side of the cloud (Fig. 13c). In addition, the net effect of entrainment is apparent in the lower tracer concentrations at this time.

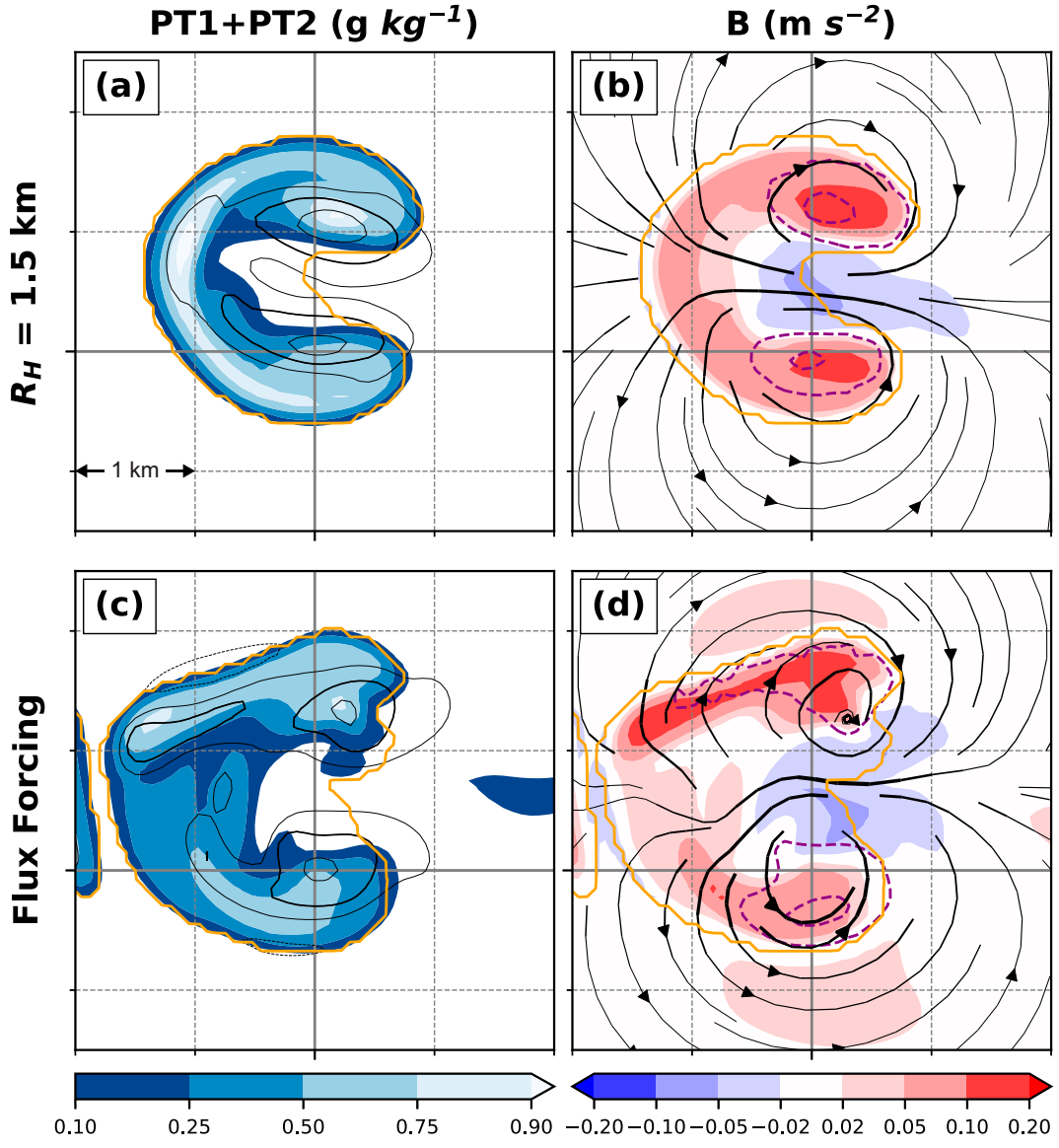

FIG. 9. A comparison of horizontal cross sections at the model level closest to $z = 4$ km (model level 54) between (a),(b) the cloud produced in the $R_H = 1.5$-km simulation at $t = 10$ min after bubble insertion and (c),(d) a large cloud selected from the SHEAR simulation at $t = 13$ h 24 min. Shown are (left) the PT1 + PT2 concentration (color fill), cloud outline (orange contour), and vertical motion (black contours, every 5 m s^{-1}) and (right) the buoyancy (color fill), cloud outline (orange), perturbation pressure (purple contours, every 0.5 hPa), and streamlines relative to the $t = 12$ h base state. The plots are centered on the updraft helicity maximum on the model level closest to $z = 4$ km, smoothed using a Gaussian filter (standard deviation = 5 points).

The cross sections presented in Figs. 12 and 13 demonstrate that wake entrainment is a highly three-dimensional process. To further elucidate the three-dimensional impacts of wake entrainment, isosurfaces of vertical motion (colored by vertical vorticity) are examined (Fig. 14). Ten minutes after the warm bubble was inserted, the deepening cloud is characterized by a complex updraft structure. There are two thermal-like structures (i.e., quasi-discrete buoyant elements characterized by overturning circulations) present near $z = 4$ and 7 km embedded within the larger updraft. These thermal-like structures are apparent in the 20 m s^{-1} vertical velocity isosurface in Fig. 14, and as maxima of vertical velocity in Fig. 12a. Despite the flow complexities associated with the thermal-like structures, counterrotating vortices are present throughout the depth of the updraft. These counterrotating vortices are especially apparent in the region between the two thermal-like elements in the 20 m s^{-1} isosurface, where two individual updrafts characterized by vertical vorticity of opposite sign are present (Fig. 14). Moreover, high buoyancy is preserved within

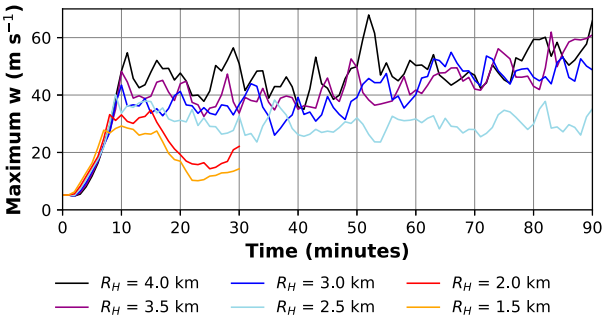

FIG. 10. A time series of maximum vertical velocity for warm bubble simulations with R_H = 1.5 (orange), 2.0 (red), 2.5 (light blue), 3.0 (blue), 3.5 (purple), and 4.0 (black) km.

the initial rising thermal, and within small columns associated with the counterrotating vortices (Figs. 12b,d). Throughout the subsequent evolution, additional rising thermals display a similar pattern of low- and midlevel wake entrainment.

To further examine the development and role of wake entrainment, parcel trajectories were calculated for the R_H = 2.5 km warm bubble simulation. Forward trajectories were seeded every 500 m in the horizontal and 250 m in the vertical within a 60 km × 60 km × 10 km box centered on the initial warm bubble location at the time the bubble was inserted. Trajectories were calculated using built-in CM1 functions at model runtime. A subset of the trajectories that achieve a vertical velocity of 10 m s^{-1} with negative buoyancy at t = 11 min after the bubble was inserted is analyzed in Fig. 15. The trajectories emphasize the presence of two entrainment mechanisms, which combine to produce the large-scale dilution apparent in Fig. 12. First, environmental parcels are entrained by the rising thermal. Several parcels pass over the cloud top and are subsequently incorporated into the updraft on the downshear side by the toroidal thermal circulation itself. This is the dynamic entrainment mechanism described in Lasher-Trapp et al. (2021). A smaller number of parcels are similarly incorporated on the upshear side of the thermal. Second, environmental parcels are incorporated into the updraft via wake entrainment in segments of the updraft between thermals. Numerous environmental trajectories travel along the cloud edge from the upshear to downshear side of the updraft and are subsequently incorporated into the updraft on the downshear side of the cloud (Fig. 15). These trajectories indicate that the air participating in the updraft originates upshear from the cloud. This pathway is consistent with the results from Knupp and Cotton (1982).

b. *Source of negative buoyancy*

One remaining uncertainty after the preceding analysis is the origin of the negative buoyancy that develops in response to wake entrainment. A negatively buoyant region is present within the downshear portion of the cloud in the SHEAR composite (Fig. 5), the SHEAR sample cloud (Fig. 8), and the clouds produced by warm bubbles (Figs. 12 and 13). It is not clear from the preceding analysis whether the negative buoyancy is a result of evaporative cooling, hydrometeor loading, or the lifting of stable environmental air. Understanding the mechanisms that result in the production of this negatively buoyant region may be useful in anticipating how wake entrainment operates in different environments (e.g., environments characterized by lower midlevel relative humidity).

The trajectories used in the analysis of the R_H = 2.5-km bubble in the previous section are used again here to examine the source of negative buoyancy within the updraft of the associated cloud. A subset of the parcels characterized by a vertical velocity > 10 m s^{-1} and buoyancy < −0.02 m s^{-2} at t = 11 min was selected. These criteria are similar to those used in Fig. 15, although the negative buoyancy threshold is more restrictive in this portion of the analysis in order to focus on parcels that obtain nonnegligible negative buoyancy. From this subset of parcels, five were selected to be representative of the wake entrainment pathway. The characteristics of these parcels provide insight into the development of the region of negative buoyancy associated with wake entrainment.

The selected parcels all originate in the midlevels of the atmosphere (between 3 and 4.25 km; Fig. 16b). After approaching the cloud, the parcels first subside for a few minutes on the flanks of the cloud (Fig. 16a). During this period of descent, the buoyancy becomes positive (Fig. 16c) as the parcels descend several hundred meters nearly dry adiabatically and therefore compressionally warm relative to their environment (Fig. 16d). Some mixing with cloudy air and evaporation into the parcels does occur during this period of descent, reflected by the slight increases in tracer concentrations (Fig. 16f) and water vapor mixing ratio (Fig. 16e).

Following the period of descent, the parcels then become incorporated into the updraft itself (via the wake entrainment pathway) and eventually all rise to above 6 km (Fig. 16b). During the first few minutes of this period of ascent, the parcels become negatively buoyant (Fig. 16c) as they remain unsaturated (Fig. 16e) and ascend nearly dry adiabatically, becoming cooler than their environments (Fig. 16d). At the time of the largest negative buoyancy, the contribution of hydrometeor loading to buoyancy is small for all five parcels (Fig. 16c); thus, hydrometeor loading is not playing a large role. Additionally, evaporative cooling is not a major factor, as the decreases in potential temperature before condensation occurs (Fig. 16e) are very slight relative to the potential temperature deficits (Fig. 16d) despite continued mixing during the period of ascent (Fig. 16f). For example, the potential temperature of parcel 197 892 (gold curves in Fig. 16) decreased only by 0.21 K relative to its initial potential temperature preceding saturation (defined here as the first instance of parcel relative humidity > 99%). However, at the same time, the parcel was 1.56 K colder than the environment, and this discrepancy can be explained as a result of the unsaturated parcel being lifted in a stable environment. Therefore, the lifting of stable environmental air, via the wake entrainment pathway, explains the region of negative buoyancy present within cloudy updrafts.

The parcels all eventually do become cloudy (Fig. 16e). Owing to mixing, saturation occurs at a lower altitude (higher pressure) than the LCLs of these parcels had they remained in the environment, as is apparent in Fig. 17. When saturation occurs, the potential temperature within the parcels begins to rise (Fig. 16d). In fact, all the parcels do eventually become positively buoyant by t = 15 min (Fig. 16c). This positive buoyancy

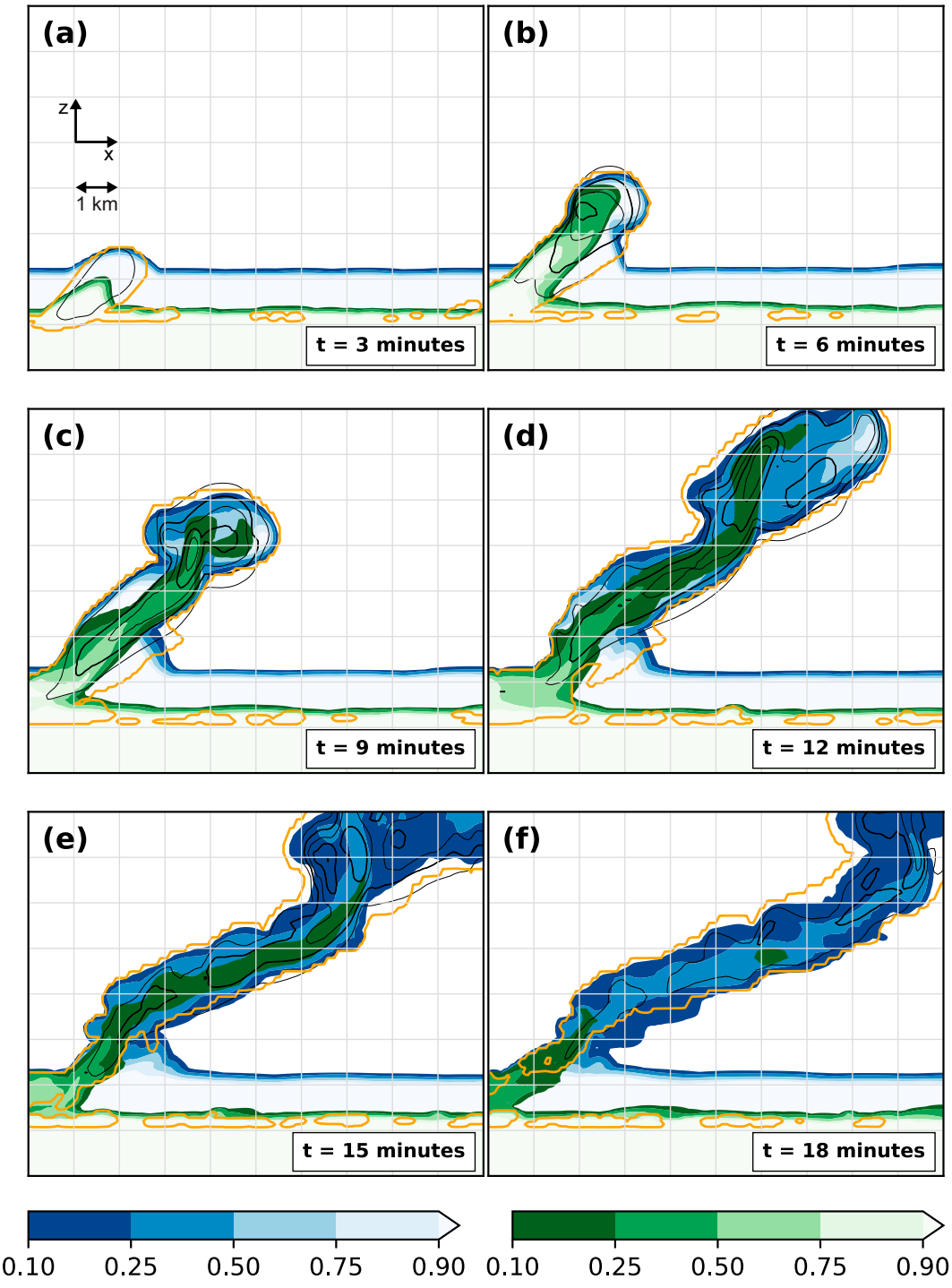

FIG. 11. The maximum tracer concentrations, calculated across the y dimension, within the R_H = 1.5-km simulation at (a) t = 3, (b) t = 6, (c) t = 9, (d) t = 12, (e) t = 15, and (f) t = 18 min. The blue shading indicates maximum PT1 + PT2 concentrations (g kg^{-1}), and the green shading indicates maximum PT1 concentrations. The orange contour indicates the 0.01 g kg^{-1} maximum cloud water content isopleth. The black contours indicate maximum vertical motion (thin contours every 5 m s^{-1}; thick contours every 10 m s^{-1}).

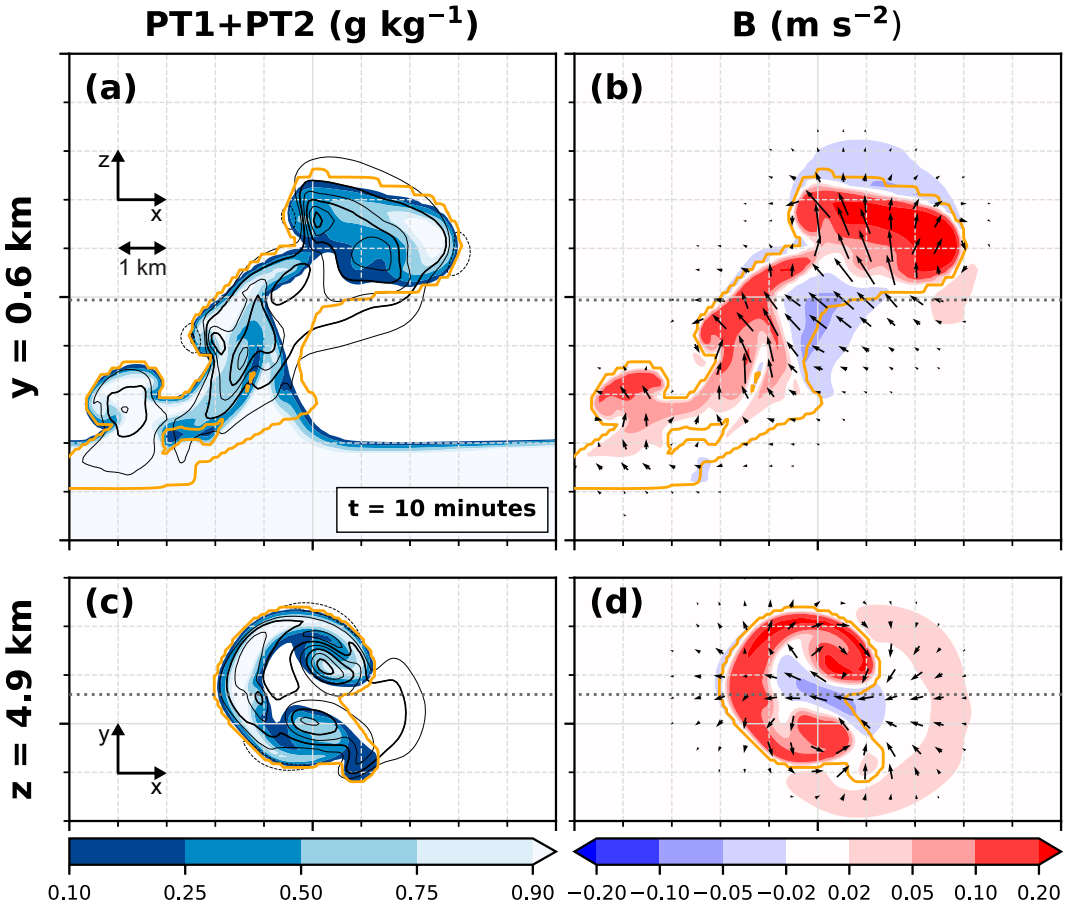

FIG. 12. Cross sections through the cloud produced in the R_H = 2.5-km simulation at t = 10 min after bubble insertion in (a),(b) the x–z plane and (c),(d) x–y plane at the closest model level to z = 5 km for (left) PT1 + PT2 concentration (blue shading, according to the color bar), vertical motion (thin black contours every 5 m s^{-1}; thick black lines every 10 m s^{-1}), and the cloud outline (orange) and (right) buoyancy (color shading, according to the color bar), perturbation winds relative to the t = 12 h base state (vectors), and the cloud outline (orange). The dashed dark-gray line in (a) and (b) shows the z location of the x–y cross section; the dashed dark-gray line in (c) and(d) shows the y location of the x–z cross section. The plots are centered on the maximum updraft helicity at the model level closest to z = 5 km (model level 61), smoothed using a Gaussian filter (standard deviation = 5 points).

occurs as the parcels become warmer than their environments (Figs. 16d and 17), despite increasing hydrometeor loading (Fig. 16c). However, the mixing of the parcels undergoing wake entrainment with parcels of air originating below 2 km plays an important role in producing this positive buoyancy. In fact, if the parcels were lifted without mixing, they would never reach a temperature greater than the environmental temperature (Fig. 17). Thus, while parcels do become warmer than their environment and positively buoyant, this only occurs at the expense of diluting parcels that contain larger buoyancy within the cloud. In this way, wake entrainment acts to reduce the buoyancy of the ascending cloud as a whole.

5. Discussion

The primary finding of this study is that the wake entrainment mechanism plays an important role in the evolution of sheared deepening cumulus clouds. Wake entrainment develops rapidly in deepening clouds (in under 10 min after a cloud begins buoyant ascent) due to the tilting of environmental horizontal vorticity associated with wind shear (summarized schematically in Fig. 18), and effectively ventilates the cloudy updraft (Figs. 5 and 6). This finding clarifies the role of wind shear on developing cumulus convection and adds context to the "P-type" circulation observed by Kitchen and Caughey (1981) and discussed by Lasher-Trapp et al. (2021). Previous research does support the conclusions that the wake entrainment mechanism develops quickly and is important in sheared cumulus convection. Consistent with the results presented here, Dahl (2017) demonstrated using an idealized modeling framework that coherent vortices associated with negative pressure perturbations of magnitudes greater than 1 hPa developed within 10 min of simulated updraft formation. The vortices produced in clouds developing from both the surface

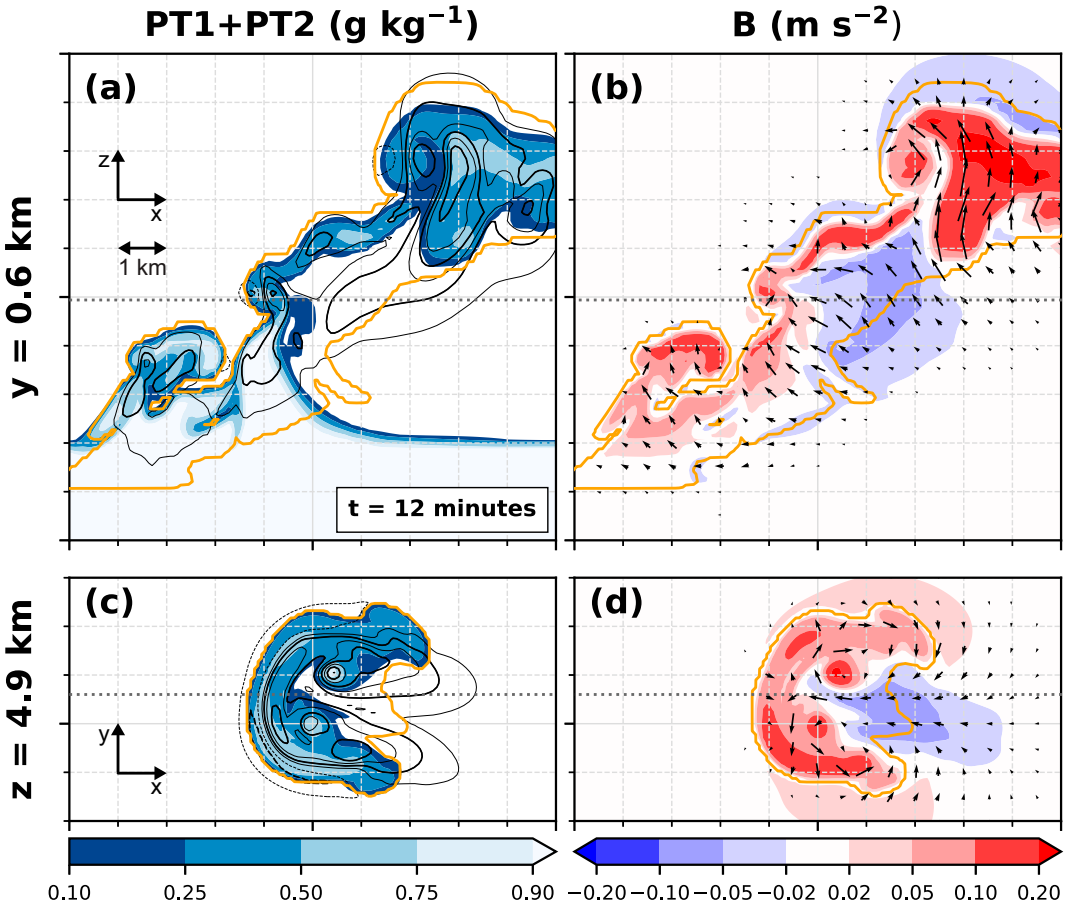

FIG. 13. As in Fig. 12, but at t = 12 min after bubble insertion.

heat flux forcing and warm bubbles were similarly associated with negative pressure perturbations of magnitudes >1 hPa (Figs. 9b,d), demonstrating an important role of the nonlinear dynamics in driving wake entrainment. This contrasts with the conclusions of Knupp and Cotton (1985), who emphasized the role of the linear pressure response (Rotunno and Klemp 1982) of an updraft in shear in addition to the vortices (Fig. 1). The role of wake entrainment supports a bottom-up mechanism for CI failure, where wake entrainment rapidly deforms and splits the updraft near cloud base (e.g., Figs. 5 and 7). For sufficiently small initial updrafts, the splitting process produces a pair of narrow updrafts that succumb to dilution and become disconnected from the CAPE-rich boundary layer, resulting in the failure of CI (Tripoli and Cotton 1980).

The mechanism of wake entrainment has been more thoroughly documented in wildfire smoke plumes, lending support to the results presented here. In a series of experiments using an array of burners, Church et al. (1980) identified "counter-rotating roll vortices" as a common feature within smoke plumes, similar to the vortices in Fig. 14. The presence of counterrotating vortices within smoke plumes was additionally demonstrated in idealized simulations by Cunningham et al. (2005) and Thurston et al. (2017), and in observed wildfire cases by Lareau et al. (2022). In some instances, the counterrotating vortices have been found to result in the "bifurcation" of the smoke plume (e.g., Church et al. 1980; Cunningham et al. 2005; Lareau et al. 2022), analogous to the updraft splitting documented here (see updraft pairs in Figs. 9, 12, and 13). The schematic diagram from Fric and Roshko (1994) (Fig. 19) is commonly referenced to demonstrate the structure of these vortices. The body of literature on wildfire smoke plumes therefore has relevance to understanding CI in wind shear and offers a unique perspective on the relevant entrainment mechanisms.

It is tempting, given the rapid updraft splitting documented here, to wonder whether wake entrainment also contributes to the *storm splitting* commonly observed in supercell storm environments, which has been attributed to upward-directed dynamic pressure gradient forces on the flanks of the initial updraft. Rotunno and Klemp (1985) noted that "the evaporation of the condensate as it comes into contact with dry midlevel air" contributes to the negative buoyancy at the center axis of the cloud before the storm splits and implicated a mechanism likely identical to wake entrainment as responsible for "bringing dry midlevel air into contact with rain and/or cloud." Rotunno and Klemp (1985) examined storm splitting with and without rain processes, and concluded that although rain processes accelerate splitting, they are not necessary for splitting. However, it is unclear how one would "turn off"

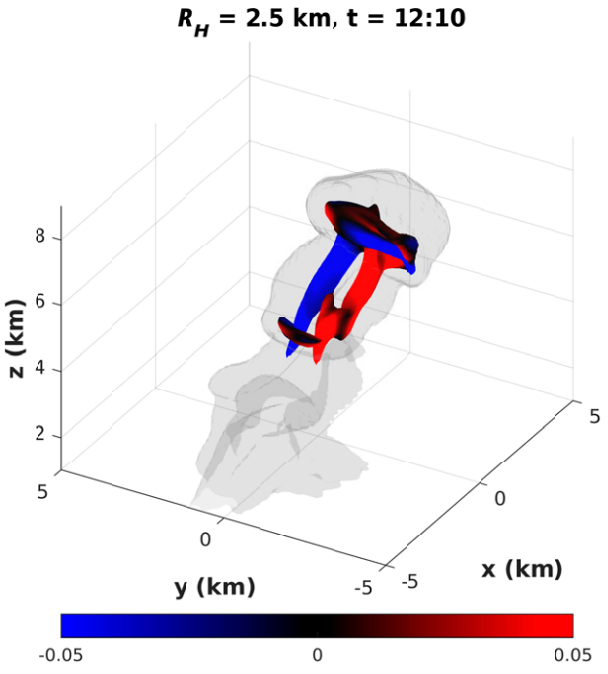

FIG. 14. Three-dimensional structure of the cloud produced in the R_H = 2.5-km simulation, at t = 10 min after bubble insertion. Isosurfaces of cloud water = 0.01 g kg^{-1} (gray) and vertical velocity = 20 m s^{-1} (colored by vertical vorticity; s^{-1}) are displayed. The figure is centered on the 2–4-km updraft helicity maximum, smoothed using a Gaussian filter (standard deviation = 2 points). The cloud is viewed from the southwest at an elevation angle of 30°.

dynamically driven wake entrainment in a study similar to Rotunno and Klemp (1985) in order to isolate its contribution to the storm-splitting phenomenon. In their study on entrainment, Lasher-Trapp et al. (2021) did not analyze the evolution of entrainment during the storm splitting process, but instead focused only on the developing and mature phases of thunderstorm evolution.

The relevance of wake entrainment to CI calls into question some of the assumptions used in the development of the Peters et al. (2022a,b) theoretical model explaining the progressive rooting mechanism for CI in the presence of wind shear. First, Peters et al. (2022a) assumed that developing clouds in shear consist of discrete thermal-like elements as in unsheared clouds, and moreover assumed that these thermal-like elements accomplish dynamic entrainment. It is demonstrated here that while thermal-like elements are present in sheared clouds and do result in dynamic entrainment (Fig. 15), the wake entrainment mechanism is especially important throughout the cloud depth and notably alters updraft properties (Figs. 5 and 6). Second, Peters et al. (2022a) assumed that lateral mixing occurs linearly with radius, and that dilution is maximized near cloud edge. Our results indicate that wake entrainment results in a more complex pattern of dilution. Wake entrainment is effective at diluting the center of the cloud itself, resulting in a marked shear-relative asymmetry in dilution (e.g., Figs. 12 and 13). It is not clear if incorporating the effects of wake entrainment would impact the results from Peters et al. (2022a,b). Our results do support the conclusion that initial updraft width is important for CI; however, the bottom-up role of shear is distinct from the shear-related feedbacks relied upon by Peters et al. (2022a,b). More research is necessary to clarify the importance of wake entrainment relative to the shear suppression effects leveraged in the progressive rooting mechanism.

An additional result from this study is that the CI attempts triggered by the surface heat flux forcing failed to produce sustained deep convection. Based on results from sensitivity tests conducted using a warm bubble initiation technique, it is

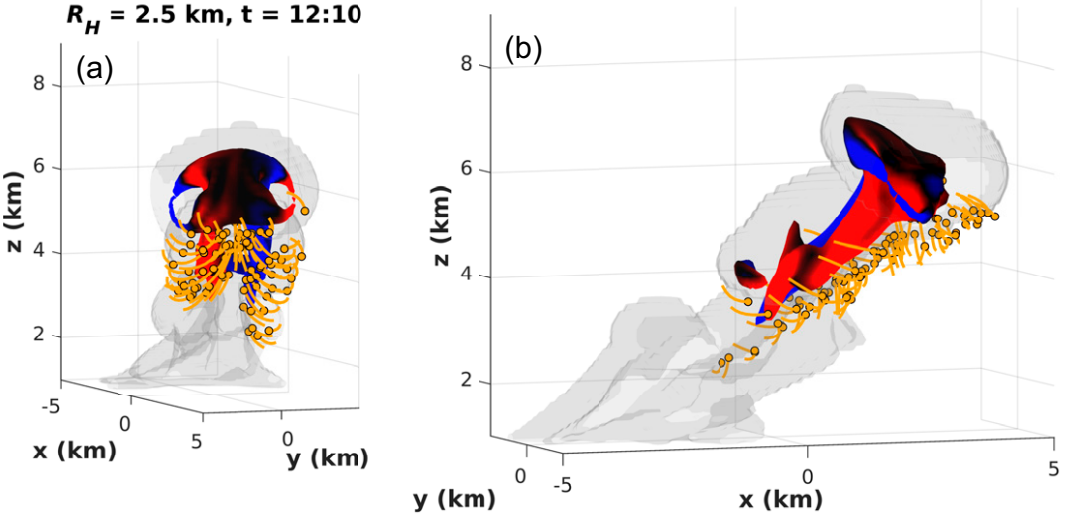

FIG. 15. As in Fig. 14, but the cloud is viewed from (a) the east and (b) the south at an elevation angle of 5°. Trajectories characterized by a vertical velocity > 10 m s^{-1} and negative buoyancy at t = 11 min are also included in (a) and (b). The orange points indicate the location of the parcel at t = 10 min, and the orange lines indicate the last minute (from t = 9 to 10 min) of storm-relative parcel motion.

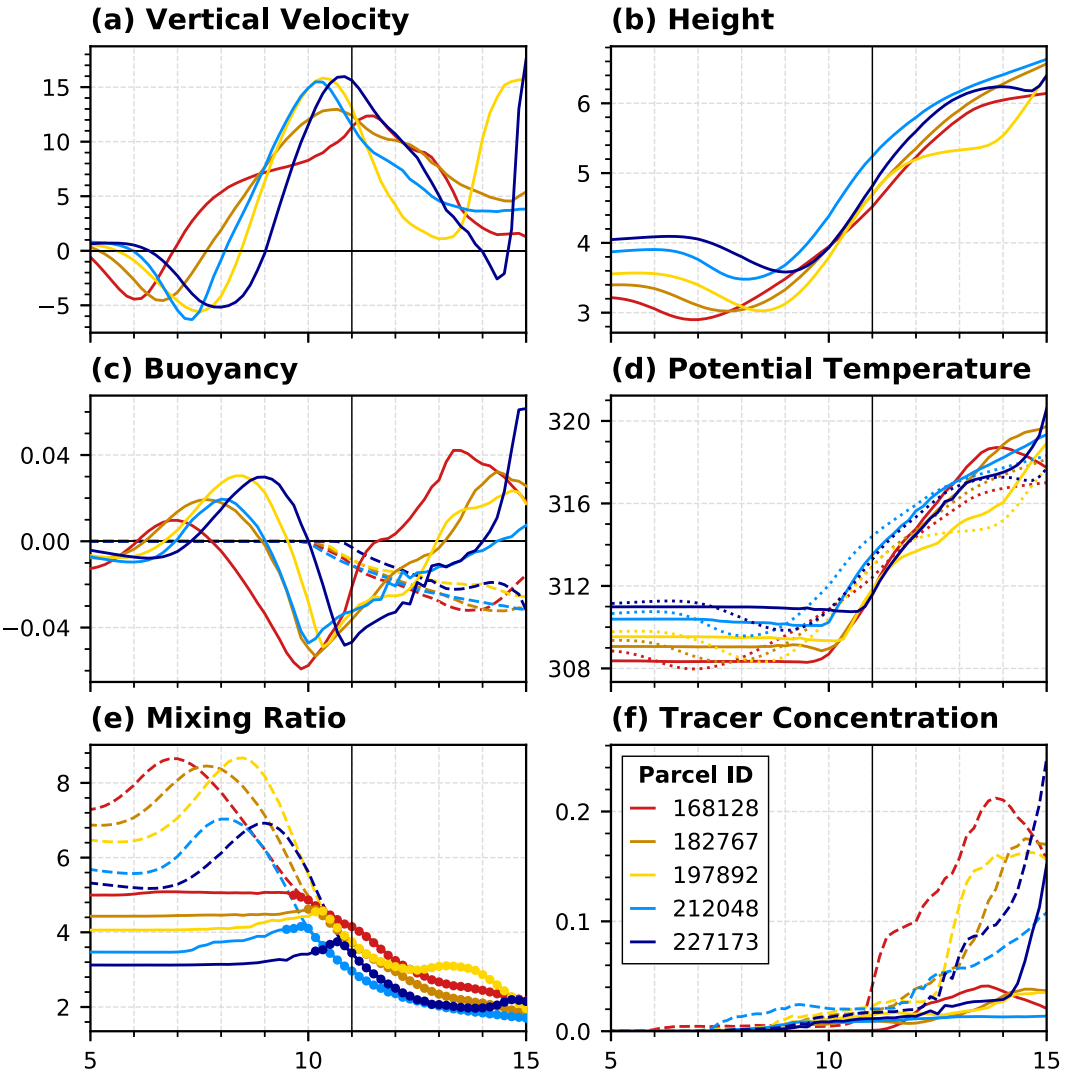

FIG. 16. The evolution of properties of five parcels characterized by vertical velocity > 10 m s^{-1} and buoyancy < -0.02 m s^{-2} at $t = 11$ min. Properties displayed include (a) vertical velocity (m s^{-1}), (b) height (km), (c) buoyancy (m s^{-2}), (d) potential temperature (K), (e) water vapor mixing ratio (g kg^{-1}), and (f) passive tracer concentration (g kg^{-1}). The dashed lines in (c) indicate the contribution to buoyancy from total hydrometeor mass. The dotted lines in (d) indicate the base-state potential temperature at the parcel height. The dashed lines in (e) indicate the saturation mixing ratio, and the dots indicate when the parcel contains nonzero cloud water mixing ratio. The solid lines in (f) indicate the concentration of PT1, and the dashed lines indicate the concentration of PT1 + PT2.

hypothesized here that sustained CI fails in the SHEAR and NOSHEAR2 simulations because the developing clouds are too narrow to survive the deleterious effects of dilution via wake entrainment (note that a weak signature of wake entrainment is apparent in the NOSHEAR2 composite, resulting from the presence of shear below 2 km). Marquis et al. (2021) found that the low-level updrafts before observed CI were 3–5-km in diameter, larger than the simulated CI attempts forced by surface heat fluxes documented here. The larger updrafts documented by Marquis et al. (2021) developed within regions of mesoscale convergence tied to terrain features. Marquis et al. (2021) hypothesized that smaller thermals may be too narrow to survive entrainment, and this hypothesis is supported by the warm bubble sensitivity tests conducted herein. Finally, the mode of CI failure may be in part due to the forcing mechanism utilized. A corridor of heating, while providing a step toward realism relative to warm bubbles, does not appear to result in initiation attempts analogous to those that occur along mesoscale airmass boundaries (or in terrain-forced ascent) in supercell environments. Real-atmosphere forcing mechanisms (such as fronts, drylines, outflow boundaries, and upslope flow) may readily produce wider, more persistent, and more repetitive updrafts that allow developing clouds to remain rooted in the boundary layer and successfully overcome wake entrainment (e.g., Marquis et al. 2021). It is possible that adjustments to the heat flux method,

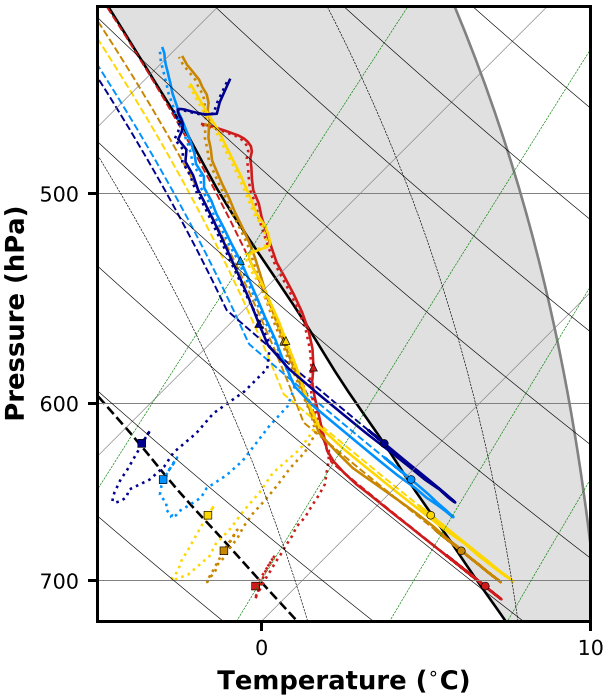

FIG. 17. The evolution of the temperature and dewpoint vs pressure of the trajectories in Fig. 16, in a skew T–log$p$ diagram. The parcel temperatures, dewpoints, and profile temperatures are indicated in color by solid lines, dotted lines, and dashed lines, respectively. The colors of the trajectories correspond to the colors in Fig. 16. The circles indicate the initial parcel temperatures, the squares indicate the initial parcel dewpoints, and the triangles indicate the parcel temperatures at $t = 11$ min. The environmental temperature and dewpoint are indicated by thick black solid and dashed lines, respectively. The thick-gray line indicates the parcel path for a surface-based parcel, and the gray-shaded region indicates the CAPE. The thin-gray grid lines are temperature and pressure. The solid black lines are dry adiabats, and the dashed black lines are moist adiabats. The dashed green lines are lines of constant water vapor mixing ratio.

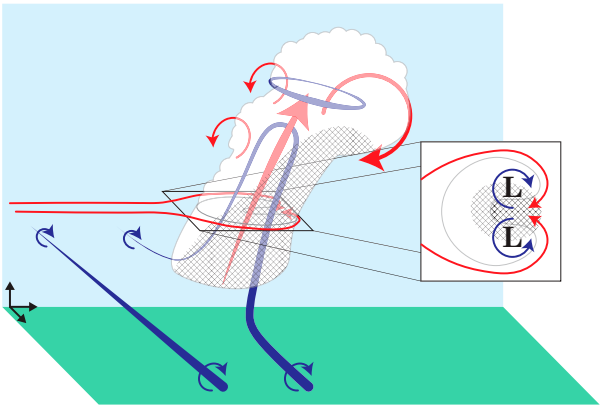

FIG. 18. A schematic diagram portraying the key features in a towering cumulus cloud in a sheared environment. The blue lines indicate vortex lines, and the blue vortex ring near cloud top indicates a thermal-like structure. The red arrows indicate flow, and the overturning red arrows indicate thermal-like circulations. The hatched area indicates the region of strong dilution, which occurs as environmental flow is entrained into the updraft on the downshear side of the tilted cloud. The inset diagram indicates the signature of wake entrainment in the horizontal plane.

such as applying the heat flux over a volume instead of only at the surface (e.g., Lasher-Trapp et al. 2021), adding a surface latent heat flux (e.g., Kang and Bryan 2011; Morrison et al. 2022; Strauss et al. 2022; Peters et al. 2022b), or increasing the magnitude or width of the surface sensible heat flux (e.g., Peters et al. 2022b) would result in CI success.

Despite the above limitations in the prescribed forcing, the conclusion that wind shear results in wake entrainment is robust across the utilized initiation mechanisms (surface fluxes and warm bubbles). There are several hypotheses resulting from this conclusion that warrant further research. First, *it is hypothesized that low-level wind shear is particularly important to CI.* Even the subset of deepening clouds in the NOSHEAR2 simulation exhibits a signature of wake entrainment in the lower portions of the composite mean cloud, indicating that wind shear *below 2 km* AGL plays a role in entrainment well *above* that level. It is therefore possible that wind shear defined across some low layer may be most relevant to CI success. Second, *it is hypothesized that the hodograph curvature may impact the potential for CI.* In the simulations presented here, the hodograph is linear above ~1 km (Fig. 2). The vortices in the flow in the SHEAR clouds are nearly symmetric, and these symmetric vortices favor the rapid and efficient ventilation of the updraft via wake entrainment (Figs. 5, 6 and 12). It is possible that, in an environment characterized by a more strongly curved hodograph or a hodograph with curvature extending over a deeper layer, one of the vortices may be favored upon or shortly after initiation (Davies-Jones 1984),[1] resulting in an asymmetry that reduces the efficiency of wake entrainment. Third, *it is possible that some threshold value of wind shear exists for the development of wake entrainment.* Understanding the range of wind shear values under which the Morrison (2017) theoretical description applies, and when it breaks down, will provide useful insight to the CI problem.

6. Summary and conclusions

CI in environments containing vertical wind shear was studied using relatively high-resolution ($\Delta x = 75$ m) numerical simulations. Two environments were used to initialize the

[1] Davies-Jones (1984) derived an expression for the correlation between vertical velocity and vertical vorticity. The correlation depends on the degree to which the horizontal vorticity in the updraft's reference frame is streamwise vs crosswise, and also on the growth rate of the isentropic surface [see his Eq. (27)]. In a growing cumulus cloud, it is possible that the large growth rate would cause the correlation between w and vertical vorticity ζ to be smaller than the correlation in a quasi-steady, mature storm. For the nearly symmetric vortices identified here, the correlation is near zero. Further research is warranted to understand the evolution of this correlation in deepening cumulus in a variety of environments.

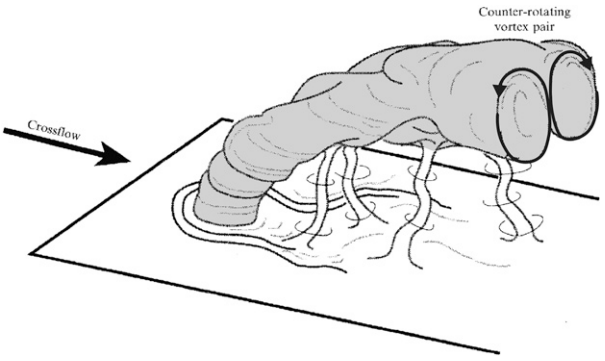

FIG. 19. A schematic diagram adapted from Fric and Roshko (1994) depicting the structure of a jet in cross-flow. The added gray shading indicates the location of the jet (analogous here to a thunderstorm updraft or smoke plume). The added black arrows indicate the sense of rotation within the counter-rotating vortices.

simulations. Both had strong boundary layer wind shear, but in the free atmosphere ($z > 2$ km), one had significant wind shear and the other had no wind shear. Both environments additionally used the same thermodynamic profile characterized by substantial CAPE and minimal CIN. When wide warm bubbles are introduced into the environments (as is commonplace in idealized simulations of convective storms), both readily allow for the development of long-lived deep convective storms. However, in simulations in which surface heat flux forcing was used to initiate convection, arguably more "naturally," long-lived storms failed to form. The simulations are extremely useful to investigate the mechanisms of CI and CI failure in the presence of wind shear, owing to the numerous CI attempts and formation of deep cumulus congestus clouds (i.e., air parcels surpassed their LFC).

The failure of sustained thunderstorm development in both simulations indicates that CI, and particularly CI in shear, is very sensitive to the forcing for initiation. Stronger, wider, and more persistent forcing may have resulted in CI success; this hypothesis was supported by the results of a series of sensitivity tests involving warm bubbles of different sizes. Additionally, although long-lived convection failed to develop in both simulations, the simulations revealed important differences in the flow patterns within the simulated deepening clouds. In particular, a flow pattern associated with a robust wake entrainment mechanism was identified in the simulation with larger wind shear. This wake entrainment was efficient at diluting the updraft of rising clouds, and therefore is hypothesized to play an important role in determining CI success and failure in the presence of wind shear. Wake entrainment appears to be particularly relevant near cloud base, and therefore results in a bottom-up failure of CI as updrafts split and narrow near cloud base and subsequently become detached from the CAPE-rich boundary layer.

The bottom-up CI failure mechanism identified herein is notably distinct from the progressive rooting mechanism of Peters et al. (2022a,b), where it was concluded that wind shear plays a role in CI through the interplay between cloud-relative flow and suppressive dynamic pressure accelerations, not buoyancy dilution. However, these two mechanisms may not be mutually exclusive, and more research reconciling the relevance of wake entrainment with the progressive rooting mechanism is necessary. Understanding the impact of wind shear on CI is of particular importance, owing to the high-impact weather that sheared deep moist convection can produce. Further research will therefore be useful to improve predictions of CI in environments supportive of supercell thunderstorms.

Acknowledgments. We thank three anonymous reviewers for their thoughtful comments that greatly improved this paper. We additionally thank Dr. Yvette Richardson and Dr. George Young for their comments on an earlier version of this paper. This work was partially supported by National Science Foundation Award AGS-2150792, and the lead author was partially supported by the Dennis and Joan Thomson Distinguished Graduate Fellowship in the Department of Meteorology and Atmospheric Science at The Pennsylvania State University (Penn State). The numerical simulations were performed on the Institute for Computational and Data Sciences Roar supercomputer at Penn State.

Data availability statement. Simulation output and code are openly available from the Penn State DataCommons (https://doi.org/10.26208/ATCP-HT11).

REFERENCES

Arnott, N. R., Y. P. Richardson, J. M. Wurman, and E. M. Rasmussen, 2006: Relationship between a weakening cold front, misocyclones, and cloud development on 10 June 2002 during IHOP. *Mon. Wea. Rev.*, **134**, 311–335, https://doi.org/10.1175/MWR3065.1.

Atkins, N. T., R. M. Wakimoto, and T. M. Weckwerth, 1995: Observations of the sea-breeze front during CaPE. Part II: Dual-Doppler and aircraft analysis. *Mon. Wea. Rev.*, **123**, 944–969, https://doi.org/10.1175/1520-0493(1995)123<0944:OOTSBF>2.0.CO;2.

Barton, E. J., C. M. Taylor, C. Klein, P. P. Harris, and X. Meng, 2021: Observed soil moisture impact on strong convection over mountainous Tibetan Plateau. *J. Hydrometeor.*, **22**, 561–572, https://doi.org/10.1175/JHM-D-20-0129.1.

Bryan, G. H., and J. M. Fritsch, 2002: A benchmark simulation for moist nonhydrostatic numerical models. *Mon. Wea. Rev.*, **130**, 2917–2928, https://doi.org/10.1175/1520-0493(2002)130<2917:ABSFMN>2.0.CO;2.

Buban, M. S., and C. L. Ziegler, 2016: The formation of small-scale atmospheric vortices via horizontal shearing instability. *J. Atmos. Sci.*, **73**, 2061–2084, https://doi.org/10.1175/JAS-D-14-0355.1.

——, ——, E. R. Mansell, and Y. P. Richardson, 2012: Simulation of dryline misovortex dynamics and cumulus formation. *Mon. Wea. Rev.*, **140**, 3525–3551, https://doi.org/10.1175/MWR-D-11-00189.1.

Church, C. R., J. T. Snow, and J. Dessens, 1980: Intense atmospheric vortices associated with a 1000 MW fire. *Bull. Amer. Meteor. Soc.*, **61**, 682–694, https://doi.org/10.1175/1520-0477(1980)061<0682:IAVAWA>2.0.CO;2.

Clark, C. A., and P. W. Arritt, 1995: Numerical simulations of the effect of soil moisture and vegetation cover on the development of deep convection. *J. Appl. Meteor. Climatol.*, **34**, 2029–2045, https://doi.org/10.1175/1520-0450(1995)034<2029:NSOTEO>2.0.CO;2.

Cotton, W. R., and G. J. Tripoli, 1978: Cumulus convection in shear flow—Three-dimensional numerical experiments. *J. Atmos. Sci.*, **35**, 1503–1521, https://doi.org/10.1175/1520-0469(1978)035<1503:CCISFD>2.0.CO;2.

Cunningham, P., S. L. Goodrick, M. Y. Hussaini, and R. R. Linn, 2005: Coherent vortical structures in numerical simulations of buoyant plumes from wildland fires. *Int. J. Wildland Fire*, **14**, 61–75, https://doi.org/10.1071/WF04044.

Dahl, J. M. L., 2017: Tilting of horizontal shear vorticity and the development of updraft rotation in supercell thunderstorms. *J. Atmos. Sci.*, **74**, 2997–3020, https://doi.org/10.1175/JAS-D-17-0091.1.

Davies-Jones, R., 1984: Streamwise vorticity: The origin of updraft rotation in supercell storms. *J. Atmos. Sci.*, **41**, 2991–3006, https://doi.org/10.1175/1520-0469(1984)041<2991:SVTOOU>2.0.CO;2.

Deardorff, J. W., 1980: Stratocumulus-capped mixed layers derived from a three-dimensional model. *Bound.-Layer Meteor.*, **18**, 495–527, https://doi.org/10.1007/BF00119502.

Doswell, C. A., H. E. Brooks, and R. A. Maddox, 1996: Flash flood forecasting: An ingredients-based methodology. *Wea. Forecasting*, **11**, 560–581, https://doi.org/10.1175/1520-0434(1996)011<0560:FFFAIB>2.0.CO;2.

Du, Y., G. Chen, B. Han, L. Bai, and M. Li, 2020: Convection initiation and growth at the coast of South China. Part II: Effects of the terrain, coastline, and cold pools. *Mon. Wea. Rev.*, **148**, 3871–3892, https://doi.org/10.1175/MWR-D-20-0090.1.

Fovell, R. G., 2005: Convective initiation ahead of the sea-breeze front. *Mon. Wea. Rev.*, **133**, 264–278, https://doi.org/10.1175/MWR-2852.1.

Fric, T. F., and A. Roshko, 1994: Vortical structure in the wake of a transverse jet. *J. Fluid Mech.*, **279**, 1–47, https://doi.org/10.1017/S0022112094003800.

Heymsfield, A. J., P. N. Johnson, and J. E. Dye, 1978: Observations of moist adiabatic ascent in northeast Colorado cumulus congestus clouds. *J. Atmos. Sci.*, **35**, 1689–1703, https://doi.org/10.1175/1520-0469(1978)035<1689:OOMAAI>2.0.CO;2.

Houston, A. L., and D. Niyogi, 2007: The sensitivity of convective initiation to the lapse rate of the active cloud-bearing layer. *Mon. Wea. Rev.*, **135**, 3013–3032, https://doi.org/10.1175/MWR3449.1.

Houze, R. A., 2014: Basic cumulus dynamics. *Cloud Dynamics*, R. A. Houze, Ed., International Geophysics Series, Vol. 104, Academic Press, 165–185, https://doi.org/10.1016/B978-0-12-374266-7.00007-X.

Kain, J. S., and Coauthors, 2013: A feasibility study for probabilistic convection initiation forecasts based on explicit numerical guidance. *Bull. Amer. Meteor. Soc.*, **94**, 1213–1225, https://doi.org/10.1175/BAMS-D-11-00264.1.

Kang, S.-L., and G. H. Bryan, 2011: A large-eddy simulation study of moist convection initiation over heterogeneous surface fluxes. *Mon. Wea. Rev.*, **139**, 2901–2917, https://doi.org/10.1175/MWR-D-10-05037.1.

Kingsmill, D. E., and R. M. Wakimoto, 1991: Kinematic, dynamic, and thermodynamic analysis of a weakly sheared severe thunderstorm over northern Alabama. *Mon. Wea. Rev.*, **119**, 262–297, https://doi.org/10.1175/1520-0493(1991)119<0262:KDATAO>2.0.CO;2.

Kitchen, M., and S. J. Caughey, 1981: Tethered-balloon observations of the structure of small cumulus clouds. *Quart. J. Roy. Meteor. Soc.*, **107**, 853–874, https://doi.org/10.1002/qj.49710745407.

Knupp, K. R., and W. R. Cotton, 1982: An intense, quasi-steady thunderstorm over mountainous terrain. Part II: Doppler radar observations of the storm morphological structure. *J. Atmos. Sci.*, **39**, 343–358, https://doi.org/10.1175/1520-0469(1982)039<0343:AIQSTO>2.0.CO;2.

——, and ——, 1985: Convective cloud downdraft structure: An interpretive survey. *Rev. Geophys.*, **23**, 183–215, https://doi.org/10.1029/RG023i002p00183.

Lareau, N. P., N. J. Nauslar, E. Bentley, M. Roberts, S. Emmerson, B. Brong, M. Mehle, and J. Wallman, 2022: Fire-generated tornadic vortices. *Bull. Amer. Meteor. Soc.*, **103**, E1296–E1320, https://doi.org/10.1175/BAMS-D-21-0199.1.

Lasher-Trapp, S., E. Jo, L. R. Allen, B. N. Engelsen, and R. J. Trapp, 2021: Entrainment in a simulated supercell thunderstorm. Part I: The evolution of different entrainment mechanisms and their dilutive effects. *J. Atmos. Sci.*, **78**, 2725–2740, https://doi.org/10.1175/JAS-D-20-0223.1.

Lee, B. D., and R. B. Wilhelmson, 1997a: The numerical simulation of non-supercell tornadogenesis. Part I: Initiation and evolution of pretornadic misocyclone circulations along a dry outflow boundary. *J. Atmos. Sci.*, **54**, 32–60, https://doi.org/10.1175/1520-0469(1997)054<0032:TNSONS>2.0.CO;2.

——, and ——, 1997b: The numerical simulation of nonsupercell tornadogenesis. Part II: Evolution of a family of tornadoes along a weak outflow boundary. *J. Atmos. Sci.*, **54**, 2387–2415, https://doi.org/10.1175/1520-0469(1997)054<2387:TNSONT>2.0.CO;2.

Lock, N. A., and A. L. Houston, 2014: Empirical examination of the factors regulating thunderstorm initiation. *Mon. Wea. Rev.*, **142**, 240–258, https://doi.org/10.1175/MWR-D-13-00082.1.

Loftus, A. M., D. B. Weber, and C. A. Doswell III, 2008: Parameterized mesoscale forcing mechanisms for initiating numerically simulated isolated multicellular convection. *Mon. Wea. Rev.*, **136**, 2408–2421, https://doi.org/10.1175/2007MWR2133.1.

Mansell, E. R., C. L. Ziegler, and E. C. Bruning, 2010: Simulated electrification of a small thunderstorm with two-moment bulk microphysics. *J. Atmos. Sci.*, **67**, 171–194, https://doi.org/10.1175/2009JAS2965.1.

Markowski, P. M., 2020: What is the intrinsic predictability of tornadic supercell thunderstorms? *Mon. Wea. Rev.*, **148**, 3157–3180, https://doi.org/10.1175/MWR-D-20-0076.1.

Marquis, J. N., Y. P. Richardson, and J. M. Wurman, 2007: Kinematic observations of misocyclones along boundaries during IHOP. *Mon. Wea. Rev.*, **135**, 1749–1768, https://doi.org/10.1175/MWR3367.1.

——, A. C. Varble, P. Robinson, T. C. Nelson, and K. Friedrich, 2021: Low-level mesoscale and cloud-scale interactions promoting deep convection initiation. *Mon. Wea. Rev.*, **149**, 2473–2495, https://doi.org/10.1175/MWR-D-20-0391.1.

Martin, W. J., and M. Xue, 2006: Sensitivity analysis of convection of the 24 May 2002 IHOP case using very large ensembles. *Mon. Wea. Rev.*, **134**, 192–207, https://doi.org/10.1175/MWR3061.1.

Morrison, H., 2017: An analytic description of the structure and evolution of growing deep cumulus updrafts. *J. Atmos. Sci.*, **74**, 809–834, https://doi.org/10.1175/JAS-D-16-0234.1.

——, J. M. Peters, A. C. Varble, W. M. Hannah, and S. E. Giangrande, 2020: Thermal chains and entrainment in cumulus updrafts. Part I: Theoretical description. *J. Atmos.*

Sci., **77**, 3637–3660, https://doi.org/10.1175/JAS-D-19-0243.1.

——, ——, K. K. Chandrakar, and S. C. Sherwood, 2022: Influences of environmental relative humidity and horizontal scale of subcloud ascent on deep convective initiation. *J. Atmos. Sci.*, **79**, 337–359, https://doi.org/10.1175/JAS-D-21-0056.1.

Nelson, T. C., J. Marquis, A. Varble, and K. Friedrich, 2021: Radiosonde observations of environments supporting deep moist convection initiation during RELAMPAGO-CACTI. *Mon. Wea. Rev.*, **149**, 289–309, https://doi.org/10.1175/MWR-D-20-0148.1.

Orlanski, I., 1975: A rational subdivision of scales for atmospheric processes. *Bull. Amer. Meteor. Soc.*, **56**, 527–530, https://doi.org/10.1175/1520-0477-56.5.527.

Parker, M. D., 2010: Relationship between system slope and updraft intensity in squall lines. *Mon. Wea. Rev.*, **138**, 3572–3578, https://doi.org/10.1175/2010MWR3441.1.

Peckham, S. E., R. B. Wilhelmson, L. J. Wicker, and C. L. Ziegler, 2004: Numerical simulation of the interaction between the dryline and horizontal convective rolls. *Mon. Wea. Rev.*, **132**, 1792–1812, https://doi.org/10.1175/1520-0493(2004)132<1792:NSOTIB>2.0.CO;2.

Peters, J. M., W. Hannah, and H. Morrison, 2019: The influence of vertical wind shear on moist thermals. *J. Atmos. Sci.*, **76**, 1645–1659, https://doi.org/10.1175/JAS-D-18-0296.1.

——, H. Morrison, A. C. Varble, W. M. Hannah, and S. E. Giangrande, 2020: Thermal chains and entrainment in cumulus updrafts. Part II: Analysis of idealized simulations. *J. Atmos. Sci.*, **77**, 3661–3681, https://doi.org/10.1175/JAS-D-19-0244.1.

——, ——, T. C. Nelson, J. N. Marquis, J. P. Mulholland, and C. J. Nowotarski, 2022a: The influence of shear on deep convection initiation. Part I: Theory. *J. Atmos. Sci.*, **79**, 1669–1690, https://doi.org/10.1175/JAS-D-21-0145.1.

——, ——, ——, ——, ——, and ——, 2022b: The influence of shear on deep convection initiation. Part II: Simulations. *J. Atmos. Sci.*, **79**, 1691–1711, https://doi.org/10.1175/JAS-D-21-0144.1.

Rotunno, R., and J. B. Klemp, 1982: The influence of the shear-induced pressure gradient on thunderstorm motion. *Mon. Wea. Rev.*, **110**, 136–151, https://doi.org/10.1175/1520-0493(1982)110<0136:TIOTSI>2.0.CO;2.

——, and J. Klemp, 1985: On the rotation and propagation of simulated supercell thunderstorms. *J. Atmos. Sci.*, **42**, 271–292, https://doi.org/10.1175/1520-0469(1985)042<0271:OTRAPO>2.0.CO;2.

Rousseau-Rizzi, R., D. J. Kirshbaum, and M. K. Yau, 2017: Initiation of deep convection over an idealized mesoscale convergence line. *J. Atmos. Sci.*, **74**, 835–853, https://doi.org/10.1175/JAS-D-16-0221.1.

Segal, M., R. W. Arritt, C. Clark, R. Rabin, and J. Brown, 1995: Scaling evaluation of the effect of surface characteristics on potential for deep convection over uniform terrain. *Mon. Wea. Rev.*, **123**, 383–400, https://doi.org/10.1175/1520-0493(1995)123<0383:SEOTEO>2.0.CO;2.

Strauss, C., D. Ricard, and C. Lac, 2022: Dynamics of the cloud–environment interface and turbulence effects in an LES of a growing cumulus congestus. *J. Atmos. Sci.*, **79**, 593–619, https://doi.org/10.1175/JAS-D-20-0386.1.

Tang, S. L., and D. J. Kirshbaum, 2020: On the sensitivity of deep-convection initiation to horizontal grid resolution. *Quart. J. Roy. Meteor. Soc.*, **146**, 1085–1105, https://doi.org/10.1002/qj.3726.

Thurston, W., J. D. Kepert, K. J. Tory, and R. J. B. Fawcett, 2017: The contribution of turbulent plume dynamics to long-range spotting. *Int. J. Wildland Fire*, **26**, 317–330, https://doi.org/10.1071/WF16142.

Trier, S. B., G. S. Romine, D. A. Ahijevych, R. A. Sobash, and M. B. Chasteen, 2021: Relationship of convection initiation and subsequent storm strength to ensemble simulated environmental conditions during IOP3b of VORTEX Southeast 2017. *Mon. Wea. Rev.*, **149**, 3265–3287, https://doi.org/10.1175/MWR-D-21-0111.1.

Tripoli, G. J., and W. R. Cotton, 1980: A numerical investigation of several factors contributing to the observed variable intensity of deep convection over South Florida. *J. Appl. Meteor. Climatol.*, **19**, 1037–1063, https://doi.org/10.1175/1520-0450(1980)019<1037:ANIOSF>2.0.CO;2.

Wakimoto, R. M., 2001: Convectively driven high wind events. *Severe Convective Storms*, *Meteor. Monogr.*, No. 50, Amer. Meteor. Soc., 255–298, https://doi.org/10.1175/0065-9401-28.50.255.

——, and N. T. Atkins, 1994: Observations of the sea-breeze front during CaPE. Part I: Single-Doppler, satellite, and cloud photogrammetry analysis. *Mon. Wea. Rev.*, **122**, 1092–1114, https://doi.org/10.1175/1520-0493(1994)122<1092:OOTSBF>2.0.CO;2.

——, and H. V. Murphey, 2010: Analysis of convergence boundaries observed during IHOP_2002. *Mon. Wea. Rev.*, **138**, 2737–2760, https://doi.org/10.1175/2010MWR3266.1.

Wang, C.-C., D. J. Kirshbaum, and D. M. L. Sills, 2019: Convection initiation aided by lake-breeze convergence over the Niagara Peninsula. *Mon. Wea. Rev.*, **147**, 3955–3979, https://doi.org/10.1175/MWR-D-19-0123.1.

Weckwerth, T. M., 2000: The effect of small-scale moisture variability on thunderstorm initiation. *Mon. Wea. Rev.*, **128**, 4017–4030, https://doi.org/10.1175/1520-0493(2000)129<4017:TEOSSM>2.0.CO;2.

——, J. W. Wilson, and R. M. Wakimoto, 1996: Thermodynamic variability within the convective boundary layer due to horizontal convective rolls. *Mon. Wea. Rev.*, **124**, 769–784, https://doi.org/10.1175/1520-0493(1996)124<0769:TVWTCB>2.0.CO;2.

Weisman, M. L., and J. B. Klemp, 1982: The dependence of numerically simulated convective storms on vertical wind shear and buoyancy. *Mon. Wea. Rev.*, **110**, 504–520, https://doi.org/10.1175/1520-0493(1982)110<0504:TDONSC>2.0.CO;2.

Wilson, J. W., and W. E. Schreiber, 1986: Initiation of convective storms at radar-observed boundary-layer convergence lines. *Mon. Wea. Rev.*, **114**, 2516–2536, https://doi.org/10.1175/1520-0493(1986)114<2516:IOCSAR>2.0.CO;2.

Xue, M., and W. J. Martin, 2006a: A high-resolution modeling study of the 24 May 2002 dryline case during IHOP. Part I: Numerical simulation and general evolution of the dryline and convection. *Mon. Wea. Rev.*, **134**, 149–171, https://doi.org/10.1175/MWR3071.1.

——, and ——, 2006b: A high-resolution modeling study of the 24 May 2002 dryline case during IHOP. Part II: Horizontal convective rolls and convective initiation. *Mon. Wea. Rev.*, **134**, 172–191, https://doi.org/10.1175/MWR3072.1.

Ziegler, C. L., and E. N. Rasmussen, 1998: The initiation of moist convection at the dryline: Forecasting issues from a case study perspective. *Wea. Forecasting*, **13**, 1106–1131, https://doi.org/10.1175/1520-0434(1998)013<1106:TIOMCA>2.0.CO;2.

——, T. J. Lee, and R. A. Pielke, 1997: Convective initiation at the dryline: A modeling study. *Mon. Wea. Rev.*, **125**, 1001–1026, https://doi.org/10.1175/1520-0493(1997)125<1001:CIATDA>2.0.CO;2.